

Meandering dynamics of streamwise vortex pairs in afterbody wakes

R. Ranjan¹†, J.-C. Robinet², D. Gaitonde¹

¹Mechanical and Aerospace Engineering, The Ohio State University, Columbus, OH 43210, USA

²DynFluid Lab. - Arts & Métiers Paris - 151, Bd. de l'Hôpital - 75013 - Paris - France

(Received xx; revised xx; accepted xx)

Wakes of upswept afterbodies are often characterized by a counter-rotating streamwise vortex pair. The unsteady dynamics of these vortices are examined with a spatio-temporally resolved Large-Eddy Simulation (LES) dataset on a representative configuration consisting of a cylinder with upswept basal surface. Emphasis is placed on understanding the meandering motion of the vortices in the pair, including vortex core displacement, spectral content, stability mechanisms and overall rank-behavior. The first two energy-ranked modes obtained through Proper orthogonal decomposition (POD) of the time-resolved vorticity field reveals a pair of vortex dipoles aligned relatively perpendicularly to each other. The dynamics is successfully mapped to a matched Batchelor vortex pair whose spatial and temporal stability analyses indicate similar dipole structures associated with an $|m| = 1$ elliptic mode pair. This short-wave elliptic instability dominates the meandering motion, with strain due to axial velocity playing a key role in breakdown. The low frequency of the unstable mode (Strouhal number $St_D \simeq 0.3$ based on cylinder diameter) is consistent with spectral analysis of meandering in the LES. The wake is examined for its rank behavior; the number of modes required to reproduce the flow to given degree of accuracy diminishes rapidly outside of the immediate vicinity of the base. Beyond two diameters downstream, only two leading POD modes are required to reconstruct the dominant meandering motion and spatial structure in the LES data with $< 15\%$ performance loss, while ten modes nearly completely recover the flow field. This low-rank behavior may hold promise in constructing a reduced-order model for control purposes.

1. Introduction

The complexity of turbulent afterbody flows is associated with presence of separation bubbles, rollup and flapping of shear layer, vortex-shear layer interactions and vortex-vortex interactions. The present work considers the situation where the afterbody is characterized by a cylinder, with axis aligned with the freestream, terminated by a planar upswept base. The configuration, shown in figure 1, is representative of the aft fuselage of a typical cargo aircraft (Morel 1978; Bulathsinghala *et al.* 2017), but the flowfield is relevant to many applications including automobiles (Lienhart *et al.* 2002; Rossitto *et al.* 2016) and high-speed trains (Bell *et al.* 2016). The configuration consists of a nose section (spherical or ogive forebody) followed by a main cylindrical section of diameter D . The trailing end of the cylinder is cut by a slanted base, whose angle with the horizontal is ϕ , giving rise to an upstream apex (UA) and a downstream apex (DA) as the extreme endpoints on the base. The range of upsweep angles typically employed in aircraft ranges

† Email address for correspondence: ranjan.25@osu.edu

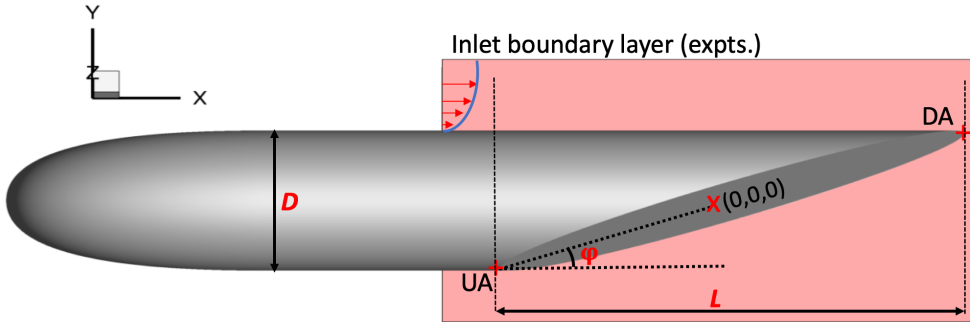


Figure 1: Canonical configuration employed to reproduce the streamwise-oriented wake vortex pair. Cylinder diameter is D and upsweep angle is $\phi = 20^\circ$. The coordinate axis origin is located at the center of the upswept surface, $(0, 0, 0)$, (red cross: \times) and the axial slant length is $L = D \cot(\phi)$. The shaded colored region encompasses the near-computational domain. The upstream apex (UA) and the downstream apex (DA) are located at $x/D = -\frac{\cot(\phi)}{2}$, $y/D = -0.5$, $z/D = 0$ and $x/D = \frac{\cot(\phi)}{2}$, $y/D = 0.5$, $z/D = 0$ respectively. To describe the flow around the upswept base, the transformation $X = x + \frac{D}{2}\cot(\phi)$ is used such that UA and DA are at $X/L = 0$ and $X/L = 1$ respectively. At the inlet, simulated boundary layer data matching the experiments (Zigunov *et al.* 2020b) are used.

from $7^\circ \leq \phi \leq 28^\circ$; we select 20° as a representative value that generates the phenomena of interest.

The overall features of the flow have been described in numerous works; the dominant feature arising from flow separation around the periphery of the base region is a streamwise-oriented vortex pair downstream (Bulathsinghala *et al.* 2017; Garmann & Visbal 2019; Zigunov *et al.* 2020b; Ranjan *et al.* 2020). For illustration and future reference, visualizations from the current Large Eddy Simulations (LES) are shown in figure 2. In figure 2(a), a Q-criterion (Haller 2005) iso-level ($Q = 30$) is depicted, colored by streamwise vorticity, ω_x , together with select superposed streamlines to provide an indication of the swirling motion in the instantaneous flow. The counter-rotating streamwise vortex pair as well as the twisting motion of each vortex in the pair, are clearly evident. Figure 2(b) displays the mean flowfield using the same flow variables. In the mean sense, each vortex in the pair gradually assumes an axisymmetric form in the region outside of the immediate vicinity of the upstream apex. § 3 and § 4 provide further insights into the mean structure of the flowfield and lay the foundation to examine the spatio-temporal features of the vortex pair as influenced by a breakdown of the separated shear layer, fluid entrainment, potential vortex-vortex interactions and meandering.

Depending on the Reynolds number, this structure persists in a range of $\phi \leq 45^\circ$; descriptions at other upsweep angles in $24^\circ \leq \phi \leq 45^\circ$ may be found in Bulathsinghala *et al.* (2017); Garmann & Visbal (2019); Zigunov *et al.* (2020b) and Ranjan *et al.* (2020). At even higher upsweep angles ($\phi > 45^\circ$) however, the flow changes to a turbulent wake regime typical of bluff-body wakes (Morel 1978; Ranjan *et al.* 2020). Hysteresis or bi-stable states are possible, typically at higher angles than that considered here (Morel 1978; Zigunov *et al.* 2020b; Ranjan & Gaitonde 2020) but these phenomena are outside the scope of the current effort.

From a practical point of view, the presence of the vortex pair results in higher drag and significant unsteadiness for long distances downstream due to the meandering (or

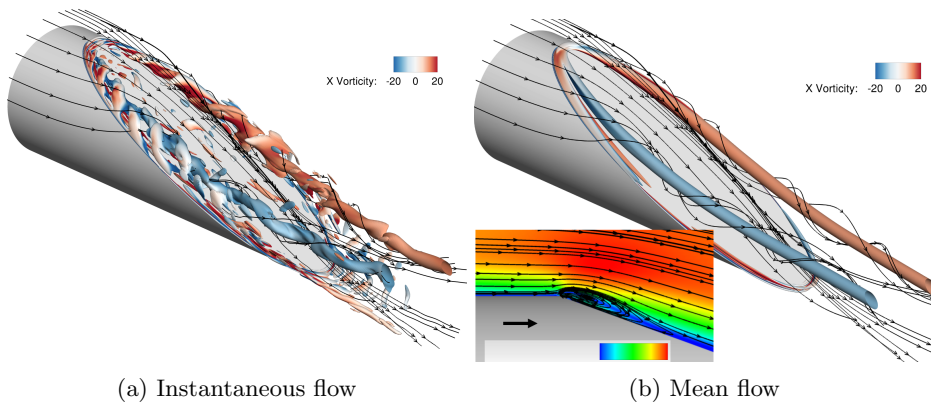


Figure 2: Longitudinal vortices behind the slanted body. An iso-surface of $Q = 30$ is plotted, colored by streamwise vorticity ω_x . The mean separation bubble near the upstream apex is shown in inset (b). The configuration is inverted with positive y -axis pointing downward for display purposes.

wandering) of vortices, both of which are major concerns for designers. For example, the unsteadiness and meandering motion can affect payload accuracy and paratrooper safety, as well as impose constraints on distance from trailing aircraft and airport operations (Holzäpfel *et al.* 2019). The overall goal of the present work is to: 1) describe the phenomenology of streamwise-oriented vortex pair dynamics, including meandering, 2) place this phenomenology in the context of stability mechanisms, and 3) examine the low-rank behavior of the complex flowfield for potential model-order reduction.

The overwhelming number of studies on axial vortex pairs representative of the aircraft fuselages have been experimental in nature. Most early studies (Morel 1978; Britcher & Alcorn 1991; Epstein *et al.* 1994; Bury *et al.* 2013) focus on more practical aspects such as drag due to upsweep angle. Recently, however, details of the unsteady motion have become clearer through experiments using advanced diagnostics and high-fidelity simulations. Bulathsinghala *et al.* (2017) performed extensive experimental studies on slanted cylindrical bodies, similar to that of figure 1 for five upsweep angles between 24° and 32° , and Reynolds numbers of $Re_D = 2 \times 10^4$ and 2×10^5 based on cylinder diameter D and free-stream velocity U_∞ . Proper Orthogonal Decomposition (POD) of flowfields from high-resolution Particle Image Velocimetry (PIV) measurements reveal clear evidence of vortex meandering, similar to that observed in wing-tip (Chow *et al.* 1997) and delta-wing (Zhang *et al.* 2016) vortices. Subsequently, Jackson *et al.* (2020) used control techniques such as continuous and pulsed jets on the same configuration to reduce drag; however, an undesirable side effect was an increase in vortex meandering. Recently, Zigunov *et al.* (2020b) also consider a similar topology at three upsweep angles $\phi = 20^\circ, 32^\circ$ and 45° , and a range of Reynolds numbers between $Re_D = 2.5 \times 10^4$ and 5×10^5 . Based on a comparison of vortex strengths at different ϕ , they observed that the core becomes weaker with the upsweep angle, and that may thus result in increased meandering. Experimental observations are generally limited to regions near the base; as such, data on the downstream evolution of vortex pair, or the dynamics of the turbulence field, is not accessible in regions where meandering can be prominent.

Fully resolved simulations have aided in filling this gap. Large Eddy Simulations (LES) were performed by Garmann & Visbal (2019) on one of the configurations of Bulaths-

inghala *et al.* (2017), specifically at $Re_D = 2 \times 10^5$ and $\phi = 28^\circ$. They characterized the meandering of vortices downstream of the body in previously unachievable detail by simulating the entire configuration, including the upstream nose region. The boundary layer transitioned in the mid-section of the cylinder with a Klebanoff-type (K-type) breakdown and eventually became turbulent near the downstream apex (see figure 1 for definition). They found that the meandering amplitude is maximum below the upswept base where there is a strong interaction of the vortex with the surface, and its value decreases with the streamwise distance. The phenomenology and dynamics of meandering in the current problem are discussed in detail in § 5.1, using a reliable vortex center detection technique. The motion of each vortex about its corresponding mean location is characterized, as are correlations between the motions. The evolution of energetic structures in the turbulent field with streamwise distance is also examined using POD in § 5.2.

The motions associated with vortex meandering are considerably broader than those observed specifically in the configuration of figure 2 and include, for example, wingtip (Del Pino *et al.* 2011) and delta-wing vortices (Ma *et al.* 2017). A consensus regarding underlying mechanisms in all these flows that sustain the displacement of vortex cores during meandering remains elusive. For example, some early efforts (Corsiglia *et al.* 1973) ascribe meandering phenomena in wind tunnels to the disturbance environment *i.e.*, free-stream turbulence effects in the test environment. This attribution was motivated by the fact that some experiments on wingtip vortices (Baker *et al.* 1974) observed coherent side-to-side motions, similar to those associated with wandering at zero angle of attack *i.e.*, when no vortices are formed. More recent experimental efforts (Devenport *et al.* 1996; Beresh *et al.* 2010) have observed that wandering amplitude increases with downstream distance, which is indicative of the possible existence of an instability mechanism.

Simplified situations with theoretical vortex models have greatly aided in developing a better understanding of the instability mechanism. Antkowiak & Brancher (2004) deduced the transient amplification of a disturbance to Lamb-Oseen vortex as being associated with the Orr mechanism as well as vortex induction. Other efforts have incorporated complications associated with external strain and the presence of a wake on the stability of the flow. The Batchelor vortex model that includes the effects of axial velocity, for example, has been fruitfully employed in some recent studies. At high swirl and Reynolds numbers, Parras & Fernandez-Feria (2007) connected the stability of these vortices to the dynamics of actual large-aircraft vortices. Through rigorous spatial stability analysis, they showed that at very high Reynolds number, absolute instabilities are present only in the presence of an axial velocity. Edstrand *et al.* (2016, 2018) used temporal and spatial stability analyses of a model Batchelor vortex resembling a tip vortex behind a NACA0012 wing. A key finding was the presence of marginal elliptic stability (Kerswell 2002) as a possible mechanism for meandering. This was also confirmed by Cheng *et al.* (2019), who examined the problem at a range of Reynolds numbers and angles-of-attack in water tunnel experiments and performed corresponding linear stability analyses of a fitted Batchelor vortex model. Optimal perturbation analysis by Navrose *et al.* (2019) for a trailing vortex system concluded that random perturbations near the wing surface, with relatively low initial energy, can non-linearly trigger vortex displacement.

While illustrative, studies on wake vortices modeled on isolated constructs of vortex models, may not fully represent the dynamics of vortex pairs, which could be either co- or counter-rotating (Fabre *et al.* 2002; Leweke *et al.* 2016). The temporal stability results of Hein & Theofilis (2004) on a pair of Batchelor vortices exhibiting long-wavelength

(Crow) instability, found stronger modification of the instability characteristics for the vortex pair system relative to the isolated vortex. For wingtip vortices, the vorticity dynamics of an isolated vortex, especially those occurring at short wavelengths, can be a good representative of counter-rotating vortex pair, because the individual vortices are well separated, typically by the wingspan. On the other hand, the afterbody counter-rotating vortices, such as those under consideration, are much closer to each other as they both are formed on the same slanted cylinder surface. Hence, it is imperative to consider both the vortices in stability studies. Such efforts, which consider both vortices in the pair, are scarce due to much higher computational cost than a single vortex, although some exceptions have been reported (Jugier *et al.* 2020). For the current afterbody configuration, interactions between the afterbody vortices in the pair were postulated to be related to low-frequency ($St_D \sim 0.4$, where St_D is the Strouhal number based on diameter) oscillations observed in experiments (Zigunov *et al.* 2020a). However, a rigorous stability analysis to confirm this conjecture is not available. The stability analysis in the present work, § 6, is therefore conducted by considering both vortices in the pair, each modeled as a Batchelor vortex. The analysis is performed at a downstream location, where a good description of the mean vortex can be obtained without much interference of the shear layer.

Although the causal dynamics is predicated on the underlying stability mechanisms and the corresponding stability modes, considerable insight may be obtained by post-processing the fully turbulent fluctuation field. Several models, as described above, are available to characterize the behavior of mean vortex fields, but those that capture the primary building block coherent structures underpinning the dynamics of meandering as well as shear layer are relatively scarce. A final contribution of the current work is therefore to propose a low-rank, large-scale fluctuating flowfield representation that describes the vortex meandering phenomenon. Such representations can be readily used to construct a reduced-order model (ROM) using Galerkin-projections (Rowley *et al.* 2004). Potential low-rank representation, and therefore the ROM of a complex turbulent flowfield, depends on the behavior of coherent structures, which are the next dominant flow features after the mean. These structures can be obtained from a suitable decomposition of the flowfield depending on the primary objective of the reduction. Among the flows of interest, Iungo *et al.* (2015) used selected dynamic mode decomposition (DMD) modes to construct a reduced-order model (ROM) for the downstream evolution and dynamics of wind turbine wakes. Similarly, Gupta & Wan (2019) used local linear stability modes of the time-averaged mean flow to develop a low-order model of wake meandering. Their model successfully predicts the increase in meandering amplitude and the advancement of the onset of meandering closer to the turbine.

In the current work, § 7, we employ the POD modes extracted in § 5.2 as a prelude to stability studies, to propose a low-rank representation for meandering. POD is an effective way to facilitate the construction of a physics-based low-rank approximation to meandering phenomena since it provides optimum convergence in extracting spatial modes and time-coefficients in terms of the time-mean energy of the flow (Aubry 1991). The current low-rank approximation approach is similar to that used in some related flows such as Mula & Tinney (2015) for a spiraling vortex filament, or Karami *et al.* (2019) for tornado-like vortices. However, in the present study, we adopt a more rigorous validation by not only considering the accuracy of the spatial structures due to these models but also their ability to recreate the actual meandering motion. This study can thus be directly relevant to the control efforts directed at reducing meandering. The models are examined at several streamwise locations downstream of the body to compare their performance.

2. Numerical Procedure

The configuration considered, shown earlier in figure 1 is a three-dimensional axisymmetric cylinder with a trailing sectional cut based on the upsweep angle $\phi = 20^\circ$. The chosen Reynolds number $Re_D = 2.5 \times 10^4$ is one of those based on the experimental campaign of Ziginov *et al.* (2020b). Although this Re is low compared to actual flight conditions, several experimentalists (Epstein *et al.* 1994; Bury *et al.* 2013; Bulathsinghala *et al.* 2019) note that the primary features of the flow behind an afterbody at a given upsweep angle of the base are largely independent of Re . High-fidelity simulations have independently confirmed this observation (Ranjan *et al.* 2020).

As shown in figure 1, x, y, z denote streamwise, vertical and spanwise directions respectively in the chosen coordinate system. All geometrical parameters are non-dimensionalized based on cylinder diameter (D) and free-stream velocity U_∞ . Axial distances are designated in terms of $L = D \cot(\phi)$, the distance between the upstream and downstream apexes, which are marked in figure 1. The vertical plane at $z = 0$ will be referred to as a mid-plane or symmetry plane.

The compressible Navier-Stokes equations are solved in a curvilinear (ξ, η, ζ) -coordinate system:

$$\frac{\partial}{\partial \tau} \left(\frac{Q}{J} \right) = - \left[\left(\frac{\partial F_i}{\partial \xi} + \frac{\partial G_i}{\partial \eta} + \frac{\partial H_i}{\partial \zeta} \right) + \frac{1}{Re} \left(\frac{\partial F_v}{\partial \xi} + \frac{\partial G_v}{\partial \eta} + \frac{\partial H_v}{\partial \zeta} \right) \right] \quad (2.1)$$

where, $Q = [\rho, \rho u, \rho v, \rho w, \rho E]^T$ denotes the solution vector, defined in terms of the fluid density ρ , Cartesian velocity components (u, v, w) and total specific energy $E = T/(\gamma - 1)M^2 + (u^2 + v^2 + w^2)/2$. Here, M is the Mach number of the flow, which is set to 0.1. γ is the ratio of the specific heats and T is the fluid temperature. $J = \partial(\xi, \eta, \zeta, \tau)/\partial(x, y, z, t)$ denotes the Jacobian of the transformation from Cartesian (x, y, z) to curvilinear (ξ, η, ζ) -coordinate system. The above governing equations are complemented by the ideal gas law, written in non-dimensional variables as $p = \rho T/\gamma M^2$. Sutherland's law is used to express fluid dynamic viscosity μ as a function of temperature T .

The computational domain as well as grid topology employed are shown in figure 3. The nose section of the body, shown in figure 1, is not simulated; instead, the inflow to the domain is placed upstream of the base at a location where experimental profiles are available. At this location, results from precursor simulations are performed on an axisymmetric body to match the experimental conditions used in Ziginov *et al.* (2020b). Viscous no-slip and zero normal pressure gradient boundary conditions are used on the cylinder surface, whereas freestream conditions were applied at the radial farfield boundary which is placed approximately $14D$ away from all surfaces. At the downstream farfield boundary, Neumann boundary condition with zero-gradient is specified for all flow variables.

A structured cylindrical grid is considered with a total of 485, 418 and 285 points in the longitudinal, radial and azimuthal directions respectively. The local mesh density is comparable to that employed by Garmann & Visbal (2019) for a much higher Reynolds number. A p -refinement study using fourth- and sixth-order compact difference schemes with sixth-order and eighth-order implicit filters, demonstrates mesh independence as discussed in Ranjan *et al.* (2020). The filter serves both to ensure numerical stability, as well as to provide an implicit subgrid closure mechanism (Mathew *et al.* 2003). Time-stepping is performed using the implicit Beam-Warming scheme (Beam & Warming 1976) with the diagonalization of Pulliam & Chaussee (1981). The simulations are performed with a constant non-dimensional time-step of $\Delta t = 2.5 \times 10^{-4}$, which is sufficient to ensure

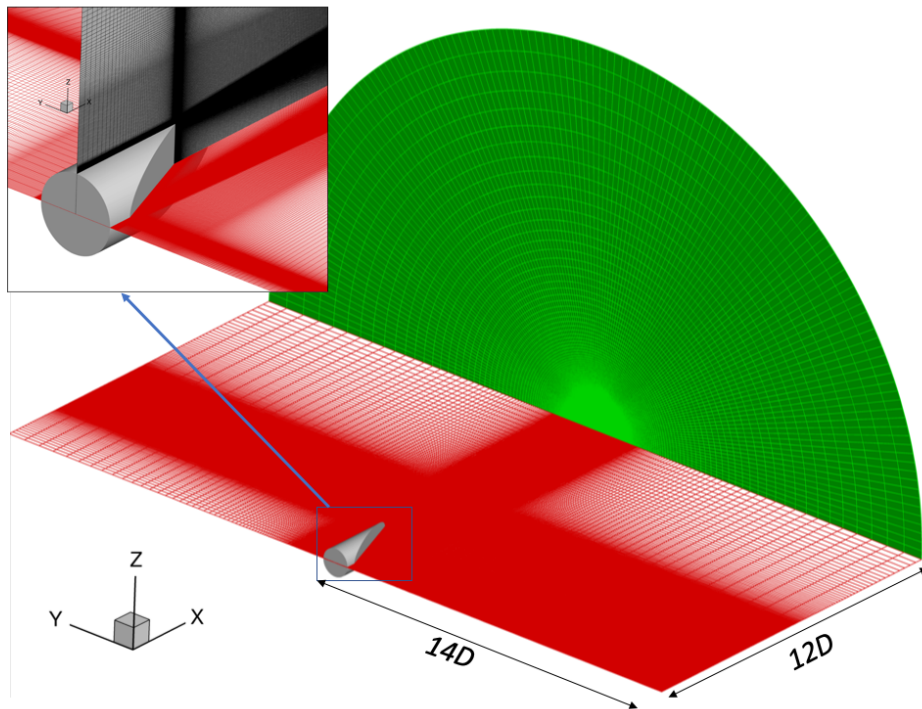


Figure 3: Computational domain and grid employed for current afterbody simulations. Grids on the center xy -plane of the base, and at downstream farfield location are shown to illustrate the grid topology. Cylindrical grid with origin at the center of the base and periodicity in the azimuthal direction is used. Domain extends $12D$ and $14D$ in downstream (green) and radial farfield (red) directions respectively. Bottom half of the computational domain is not shown.

temporal accuracy. Further details of the numerical algorithm used for the simulations can be found in Gaitonde & Visbal (1998); Visbal & Gaitonde (2002).

3. Overview of Flowfield

The representative three-dimensional instantaneous and mean flow structures were shown earlier in figure 2. The latter was obtained by computing the time average over 700,000 snapshots encompassing total non-dimensional time of $T_c \equiv tU_\infty/D = 175$. The turbulent flowfield arises as a result of the strong interaction between the separating shear layer and vortices in the region adjacent to the upswept base. Looking downstream, the left and right vortices have dominantly positive and negative streamwise vorticity components respectively. In the instantaneous flow, figure 2(a), there are smaller convecting structures that are washed out in the time-averaged sense (figure 2(b)).

The formation of the vortical structures may be summarized as follows. The boundary layer approaching the edge separates around the entire periphery to form a shear layer. The segment separating near the upstream apex rolls up to form a bubble structure in the symmetry plane (shown in the inset of figure 2(b)). The flow separating around the periphery is entrained into each vortical structure. The continuity of the vortex on the symmetry plane permits an alternative description of the vortex pair as leg components

of a single horseshoe-like vortical structure. Each vortex leg then lifts away from the upswept base, at about the midway point to form the streamwise oriented pair. After the vortices orient away from the surface, the free shear layer arising from separation at the downstream apex continues to entrain fluid into the vortices for some distance behind the body. This interaction, although not crucial in the formation phase of the vortices, affects the motion downstream.

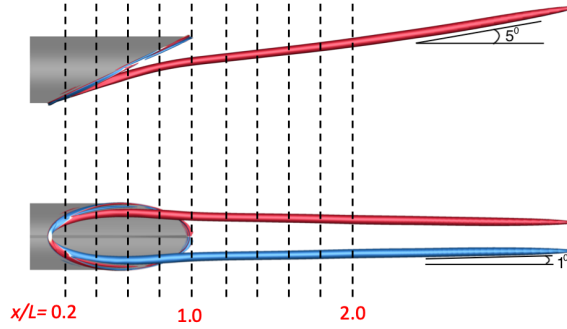
A granular description of the formation of the vortex pair is now provided for reference. The mean trajectory of the vortices is displayed using side and bottom views in figure 4(a), again with the same isolevels as in figure 2. The side view indicates that after a streamwise turn immediately after lifting off from the base, the vortex remains inclined to the freestream at an approximate angle of 5° even far downstream. The bottom view shows that the two mean vortices approach each other at a very small angle of approximately 1° towards the symmetry plane.

Figures 4(b) and (c) show the mean and instantaneous streamwise vorticity components, respectively, using cross-sectional contours at ten different locations between $0.2 \leq X/L \leq 2.0$, marked by dotted lines in figure 4(a). The mean vorticity field at $X/L = 0.2$ displays a teardrop-shaped structure, with opposing signs in the dominant lobes, which are located symmetrically about the mid-plane, $z = 0$. For future reference, the two vortices in the pair are designated as **L** and **R** vortex based on whether, looking downstream, they are located to the left or right of the symmetry plane respectively. Each vortex in the pair on the base is fed by the shear layer and gradually evolves into an axisymmetric structure at about $X/L \sim 0.6$. As evident from (a), the vortex detaches from the surface; thus the connection with the feeding sheet is clearly weaker at $X/L = 0.8$.

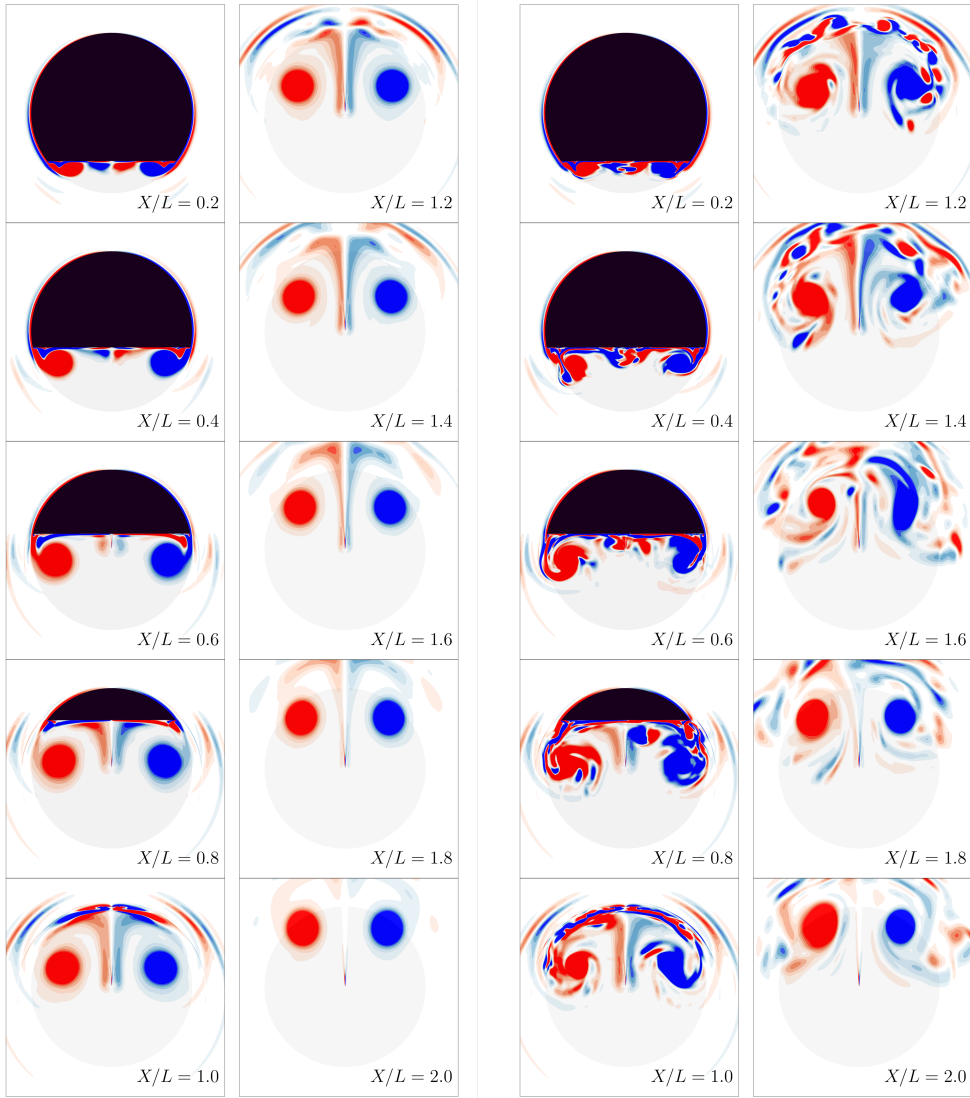
At the downstream apex of the upswept base ($X/L = 1.0$), the vortices are completely detached from the surface and the direct effect of the base shear layer on the fully developed mean vortex pair gradually diminishes. The process continues with streamwise distance with the vortices becoming essentially independent from the immediate effects of the base. Secondary and tertiary vortices are also present beneath the primary vortex, as clearly evident in planes intersecting the base. These have opposite and same signs, respectively, as the corresponding primary vortex in the pair and their influence far downstream of the base appears to be a higher-order effect. Further details of these mean flow features for ϕ values of 20° , 32° and 45° , together with various aspects of the flow on the base plane, such as surface oil flow and pressure patterns, as well as drag, have been discussed extensively in Ranjan *et al.* (2020).

Instantaneous structures of the vortices, as well as their meandering downstream, are shown in figure 4(c) on the same planes as in (b) for a representative snapshot. Although the flow is unsteady and turbulent along the entire base region, the instantaneous flow displays the dominant signature of primary vortices, consistent with figure 2(a). However, the axisymmetric nature is not evident, and the meandering of vortices is discernible in the streamwise vorticity field from $X/L = 0.8$ downstream as a result of interactions with the shear layer. Animations indicate a swirling motion of the vortex center with time, as discussed further in § 5.

Each vortex contains some regions of opposite-signed (secondary) vorticity field, these have some similarity to the ‘‘vortical substructures’’ described in Gordnier & Visbal (2005), who note their presence around the primary cores of delta-wing vortices. Their genesis is associated with the vortex-surface interaction and eruptions from the boundary layer on the upswept base surface. Their influence on the unsteady motion is significant near the base of the bluff body, as they interact with the primary vortices (Yaniktepe & Rockwell 2004; Gursul *et al.* 2005). Downstream of the base, these interactions diminish,



(a) Streamwise vortices using Q -criterion.



(b) Mean

(c) Instantaneous

Figure 4: Evolution of streamwise vortex along the base of the upswept surface through ω_x contours at 11 levels between -3 and 3. Crossflows in the intervals for 0.2 between $X/L = 0.2$ and 2.0 for the mean (b) and a representative snapshot (c) are shown. (a) shows the locations in front and top view of vortices.

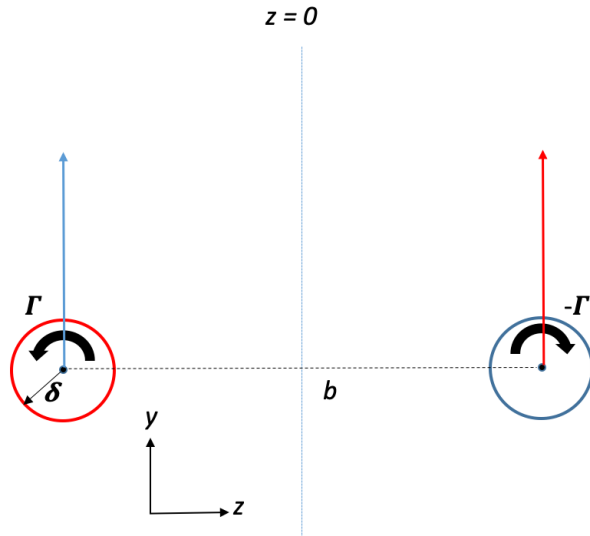


Figure 5: Pair of counter-rotating vortices at a streamwise location. δ -radius and $|\Gamma|$ -circulation of vortex. b -separation between vortices.

and between $X/L = 1.2$ and $X/L = 2.0$, a perceptible decrease of intensity in the meandering is evident, as the effects of the near-surface interactions diminish. The entrainment of flow separating at the downstream apex into the central region between the vortex cores continues until further downstream. These observations are generally consistent with those of Garmann & Visbal (2019), who performed LES of the entire configuration (including forebody) at a higher Reynolds number of $Re_D = 2.0 \times 10^5$.

4. Characterization of Mean Vortex Pair

The mean vortex pair is discussed in a canonical sense to identify key parameters of interest; this also sets the stage for subsequent examination of underlying instability mechanisms. The afterbody flow on the slanted cylinder presents a classical counter-rotating vortex pair of equal strength, shown schematically in figure 5. The main parameters of interest are the radius of the vortex core, δ , the distance between the centroids of the vortices, b , and the circulation of the vortices, Γ . The **L** and **R** vortices thus lie at $X_L = -b/2$ and $X_R = b/2$ symmetrically about the midplane.

The coordinates of the vortex centers are a primary quantity in the spatial evolution of the mean vortices (Lombard *et al.* 2016). In the literature on flow behind afterbodies, the maximum value of the Q -criterion (Bulathsinghala *et al.* 2017) or entropy (Garmann & Visbal 2019) is typically used to identify the core center. In this work we use the Γ_1/Γ_2 approach proposed in Graftieaux *et al.* (2001), employed previously by Bell *et al.* (2016) and concurrently by Ranjan *et al.* (2020); Ziguonov *et al.* (2020b). The method provides the center and boundary of a vortex by considering the local convection velocity field in the region of interest. Once the vortex is identified, the circulation may be computed using the area integral of vorticity.

Figure 6(a,b) respectively plot the vertical and spanwise locations of the **L** and **R** vortex cores. Figure 6(a) indicates that both vortices develop in the same manner along the streamwise distance, x , as anticipated, and in fact, Figure 6(b) displays symmetry about $z = 0$. A closer examination reveals that after the formation of the tear-drop

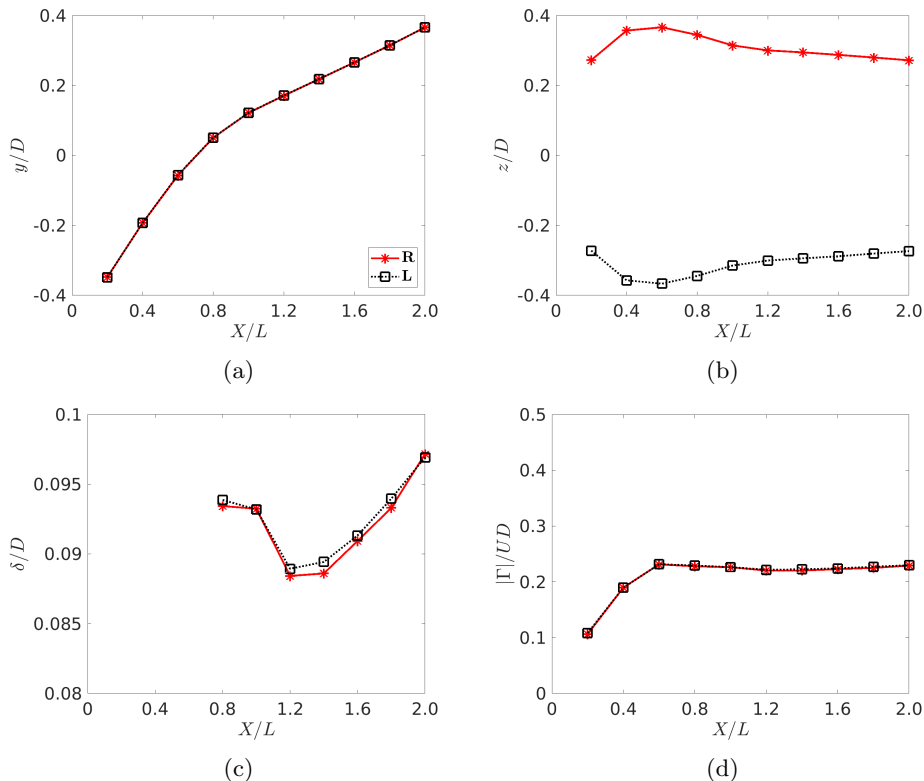


Figure 6: Mean streamwise vortex location at different X/L . (a) Vertical location, (b) Spanwise location, (c) Radius and (d) Circulation of the core.

shaped vortex at $X/L = 0.2$, the distance between the vortices grows until $X/L \sim 0.6$. This is consistent with the peripheral development of the 3D vortex structure shown in figure 2(b). Beyond $X/L \sim 0.6$, the centers approach each other until $X/L \sim 1.0$ as they conform to the elliptic shape of the base. Further downstream, beyond $X/L \sim 1.2$, the vortices achieve an asymptotic state inclined at about 5° to the free-stream flow (see figure 4(a)). For future reference, the precise inter-vortical separation, b , is reported as a function of x in Table 1, along with several other properties discussed below.

Figures 6(c) and (d) depict the evolution of the radius and circulation of each vortex leg. The radius of the vortex, δ , is plotted only after it is fully developed and becomes axisymmetric at $X/L \sim 0.6$. Figure 6(c,d), show that both **L** and **R** vortices nearly overlap, indicating acceptable convergence of the mean. Thus, both vortices are nearly identical except for the fact that they are counter-rotating in nature. The results also indicate that both the area as well as circulation increase until $X/L \sim 0.6$, *i.e.*, in the region where the vortex is fed through the shear layer (see figure 4(a)). Once the vortex lifts away from the surface and gradually becomes axisymmetric, both radius and circulation decrease. The slight increase beyond $X/L = 1.2$ is associated with the entrainment of separated fluid from the downstream apex. For completeness, the radius and circulation of the mean vortex are tabulated in Table 1.

In addition to the kinematic nature of the vortex pair, examined through the velocity field and its variants, key insights into the structure emerge from an analysis of the Reynolds stress distribution. For example, in the context of wingtip vortices, Zeman

$\frac{X}{L}$	$\frac{\delta}{D}$	$\frac{b}{D}$	$\frac{\delta}{b}$	$\frac{ \Gamma }{UD}$
0.2	-	0.5450	-	0.1070
0.4	-	0.7143	-	0.1895
0.6	-	0.7333	-	0.2315
0.8	0.0935	0.6893	0.1356	0.2288
1.0	0.0932	0.6297	0.1480	0.2262
1.2	0.0884	0.6010	0.1471	0.2210
1.4	0.0886	0.5890	0.1504	0.2218
1.6	0.0909	0.5761	0.1578	0.2234
1.8	0.0933	0.5607	0.1664	0.2255
2.0	0.0972	0.5456	0.1781	0.2295

Table 1: Properties of mean vortex at different streamwise locations. Note that there is less than 1% difference between left and right vortices in computation of parameters such as δ and $|\Gamma|$. The reported quantities are thus averaged between the two. See sketch 5 for definitions of parameters.

(1995) found that vortical structures suppress the Reynolds shear stress and therefore the vortex-core growth rate is controlled only by molecular viscosity; as such, vortex turbulence decays with distance. Figure 7 shows the distribution of normal and shear stresses on the yz -plane near the vortex pair at the location $X/L = 2.0$. The normal stresses, figure 7(a-c) are symmetric about the mid-plane as expected. $\overline{v'v'}$ and $\overline{w'w'}$ are almost equal in magnitude (maximum non-dimensional value is 0.08) and considerably larger than $\overline{u'u'}$. Also, the distributions of $\overline{v'v'}$ and $\overline{w'w'}$ are elliptic in nature, with major axes oriented in the respective directions of the fluctuations.

The shear stresses (figure 7(d-f)) are an order-of-magnitude smaller than the normal stresses and hence are plotted on a different scale. Reynolds shear stress mediates the extraction of energy from the mean flow by turbulence, and therefore in all the stresses, the peak is off-center due to zero turbulence production at the centerline of the vortex (Zeman 1995). The structure of in-plane shear stress, $\overline{v'w'}$, shows four lobes, similar to those obtained in Zeman (1995) for a turbulent wing tip vortex in the farfield region, using both Reynolds stress closure model as well as through experiments. The structures of correlating in- and out-plane shear stresses, $\overline{u'v'}$ and $\overline{u'w'}$ have additional noteworthy features. These stresses indicate the strain in the field due to fluctuations in the axial velocity. Briefly, these stresses show two-lobe structures similar to $|m| = 1$ elliptic modes (Kerswell 2002). These manifestations are associated with displacements of vortex cores as discussed later. The shear stresses are anti-symmetric with respect to the mid-plane due to the counter-rotating nature of vortices.

5. Meandering of Streamwise Vortices

5.1. Phenomenology

The motion of each vortex is now discussed by examining their behavior at location $X/L = 2.0$, where the immediate effects of the base region have diminished. The definition of vortex meandering follows Green & Acosta (1991) who characterize it as the fluctuation of the vortex core with time at a specific downstream location. The locus of vortex cores in time is presented in the form of a phase portrait in figure 8. The trajectory of each

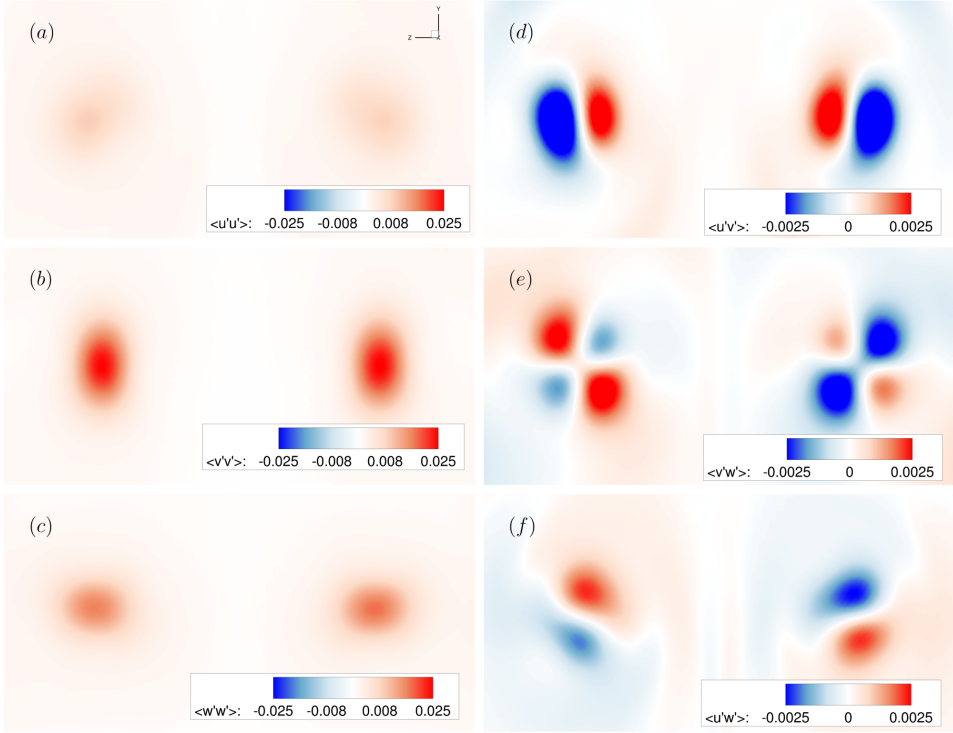


Figure 7: isolines Reynolds stresses at $X/L = 2.0$ in yz -plane. (a): $\langle u'u' \rangle$; (b): $\langle v'v' \rangle$; (c): $\langle w'w' \rangle$; (d): $\langle u'v' \rangle$; (e): $\langle v'w' \rangle$; (f): $\langle u'w' \rangle$.

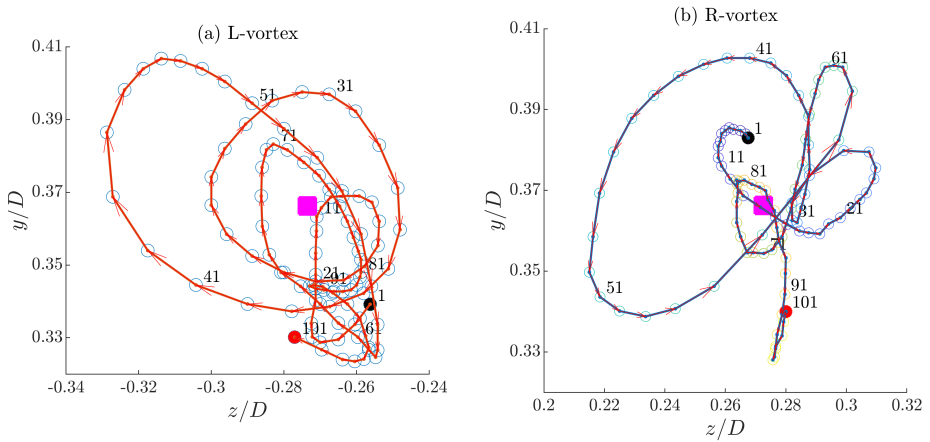


Figure 8: Phase-portrait of instantaneous vortices at $X/L = 2.0$. The location of the mean vortex is shown as the large filled square. Black and red circles respectively indicate the beginning and end of the trajectory.

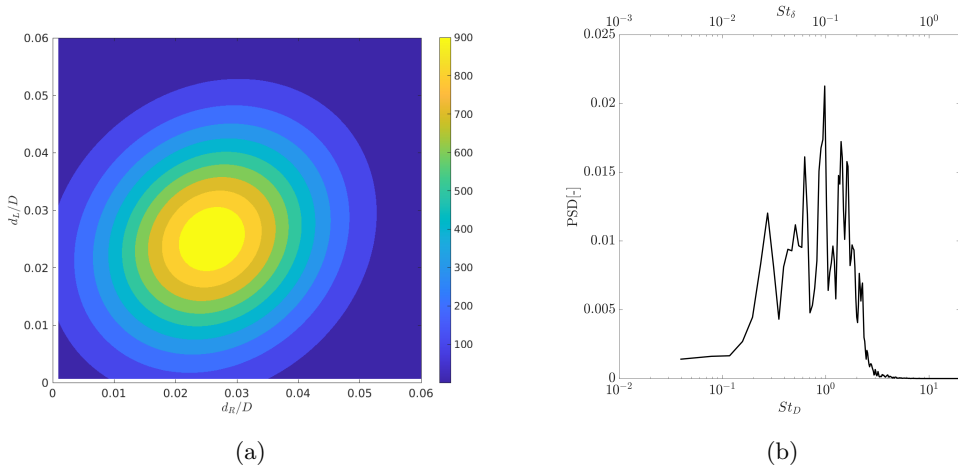


Figure 9: Characterization of streamwise vortices at $X/L = 2.0$. (a) Gaussian joint PDF of instantaneous vortices. (b) Spectral content in vortex core fluctuations using Welch PSD for the **R**-vortex. Non-dimensional frequencies are shown based on the cylinder diameter, $St_D = \frac{U_\infty D}{\nu}$ as well as vortex core diameter, $St_\delta = \frac{U_\infty \delta}{\nu}$.

core using 100 snapshots, separated by a non-dimensional time $\Delta t = 0.025$, is shown on the crossflow (yz) plane. The initial and final positions of each core are marked with black and red circles, and the position of the mean vortex core is shown as a large magenta square. While the core of the **L**-vortex meanders in the clockwise direction, the meandering trajectory of the **R**-vortex is counter-clockwise. The sense of rotation is the same as the swirl of the vortex, similar to observations on delta wings (Gordnier & Visbal 2005). The instantaneous location of each vortex core deviates significantly from the mean, with $\Delta d_{max}/D = 0.05$, where Δd_{max} is the maximum displacement of instantaneous core location from the mean. In order to quantify this phenomenon, the meandering amplitude a_m , defined as the average of distance between instantaneous core (z_i, y_i) and mean core locations (z_c, y_c) , is measured:

$$a_m = \sqrt{\frac{1}{N} \sum_{i=1}^N (z_i - z_c)^2 + (y_i - y_c)^2} \quad (5.1)$$

a_m values are 0.0288 and 0.0282 for **L** and **R** vortex, respectively. Similar values of the amplitude for both the vortices indicate their statistically analogous behavior despite seemingly random motion.

In order to estimate the correlation between meandering in the two vortices, we compute the correlation coefficient, R , between **L** and **R** vortex by using the displacements of instantaneous cores from their respective mean positions. Smaller values of this coefficient indicate lower influence of the vortices on one another. The correlation coefficient thus obtained by considering 3,000 instantaneous vortices is $R = 0.1622$. This value is very near to that reported by Jackson *et al.* (2015), but slightly higher than that of Bulathsinghala *et al.* (2017). According to Jackson *et al.* (2015), these observations are rather independent of the streamwise location. To further probe the nature of the correlation, the Gaussian joint probability distribution function (JPDF) is plotted in figure 9(a). The maximum probability of the interaction between the two vortices is observed at $d_L/D = d_R/D \simeq 0.028$. Since the mean vortices are separated by $b/D \simeq 0.06$,

a reasonable inference is that the interaction may only become important when the instantaneous vortices are closest to the symmetry plane. The JPDF diminishes as the vortices move away from the symmetry plane. Although the above analysis suggests the effects of vortices on one-another are weak, these calculations do not include the crucial axial velocity component that can play a significant role in determining the instability mechanism responsible for the meandering of these vortices as discussed in section 6.

The frequency of the meandering motion at this location is characterized using the spectral signature of the instantaneous vortices at the mean vortex core location. Figure 9(b) shows the power spectral density (PSD) of fluctuations of v -velocity for the **R**-vortex using a long time-series signal, $tU_\infty/D > 60$. The signal shows a frequency band in Strouhal number based on diameter $St_D \equiv fD/U_\infty \in [0.3 \ 2.0]$, with several low ($St_D \simeq 0.3, 0.6$) and high ($St_D \simeq 1.0, 1.4, 1.6$) frequency peaks. The maximum spectral energy is observed at $St_D \simeq 1.0$. Though not shown for brevity, similar frequency content is also obtained for the **L**-vortex. High-frequency peaks in the range $St_D \in [1.4 \ 1.6]$ were also observed in the LES studies at high Reynolds number (Garmann & Visbal 2019), whereas Zigunov *et al.* (2020a) reported strong tones at low-frequency, $St_D \simeq 0.4$, in addition to the high-frequency peaks for a range of Reynolds numbers. Zigunov *et al.* (2020a) postulated the high-frequency content to be related to the shear layer downstream of the body, while the low-frequency fluctuations were conjectured to be related to interactions between the cores as observed in several vortex meandering studies (Edstrand *et al.* 2016; Devenport *et al.* 1996). Detailed stability analyses of vortex pair are performed in §6 to investigate the vortex-vortex interactions, including effects on underlying frequency content as well as their correlation.

5.2. Coherent Structures

The phenomenon of meandering is associated with the motion of coherent structures constituting the vortex (Devenport *et al.* 1996). One approach to educe these is with proper orthogonal decomposition (POD) using the method of snapshots as introduced by Sirovich (1987). For a given unsteady flowfield, the technique extracts modes with the largest energy content, which are often related to the coherence in the flow. The POD decomposition of time snapshots, represented by $\mathbf{q}(\mathbf{x}, t)$, is given by:

$$\mathbf{q}(\mathbf{x}, t) = \bar{\mathbf{q}}(\mathbf{x}) + \sum_{i=1}^{\infty} \sqrt{\Lambda_i} \Phi_i(\mathbf{x}) \mathbf{a}_i(t) \quad (5.2)$$

where $\bar{\mathbf{q}}(\mathbf{x})$ is the mean flow. $\Phi_i(\mathbf{x})$ and $\mathbf{a}_i(t)$ represent the i^{th} orthonormal spatial mode and its time-coefficient respectively. Λ_i is the energy associated with the i^{th} POD mode.

The role of coherent structures during the development of streamwise vortices is analyzed first, as this provides a perspective of the meandering process downstream. This analysis is thus performed at different streamwise sections along the upswept base. 3,000 snapshots, sampled every 100 iterations, are collected, for an effective time-step $\Delta t_{\text{POD}} = 0.025$. Results performed for each vortex in isolation indicate very similar spatial dynamics due to flow symmetry. For brevity, results from only **R**-vortex are presented here.

The first two most energetic modes are shown along with the mean vortex in Figure 10 at three different sections along the ramp, namely at $X/L = 0.2, 0.6$ and 1.0 . At $X/L = 0.2$, figure 10(a), where the mean vortex is in a nascent stage and fed by the shear layer, the first mode qualitatively resembles the mean field (Bulathsinghala *et al.* 2017). This indicates the prominence of fluctuations in both the vortex as well as the shear layer. Proceeding downstream, at $X/L = 0.6$ in figure 10(b), where the mean vortices

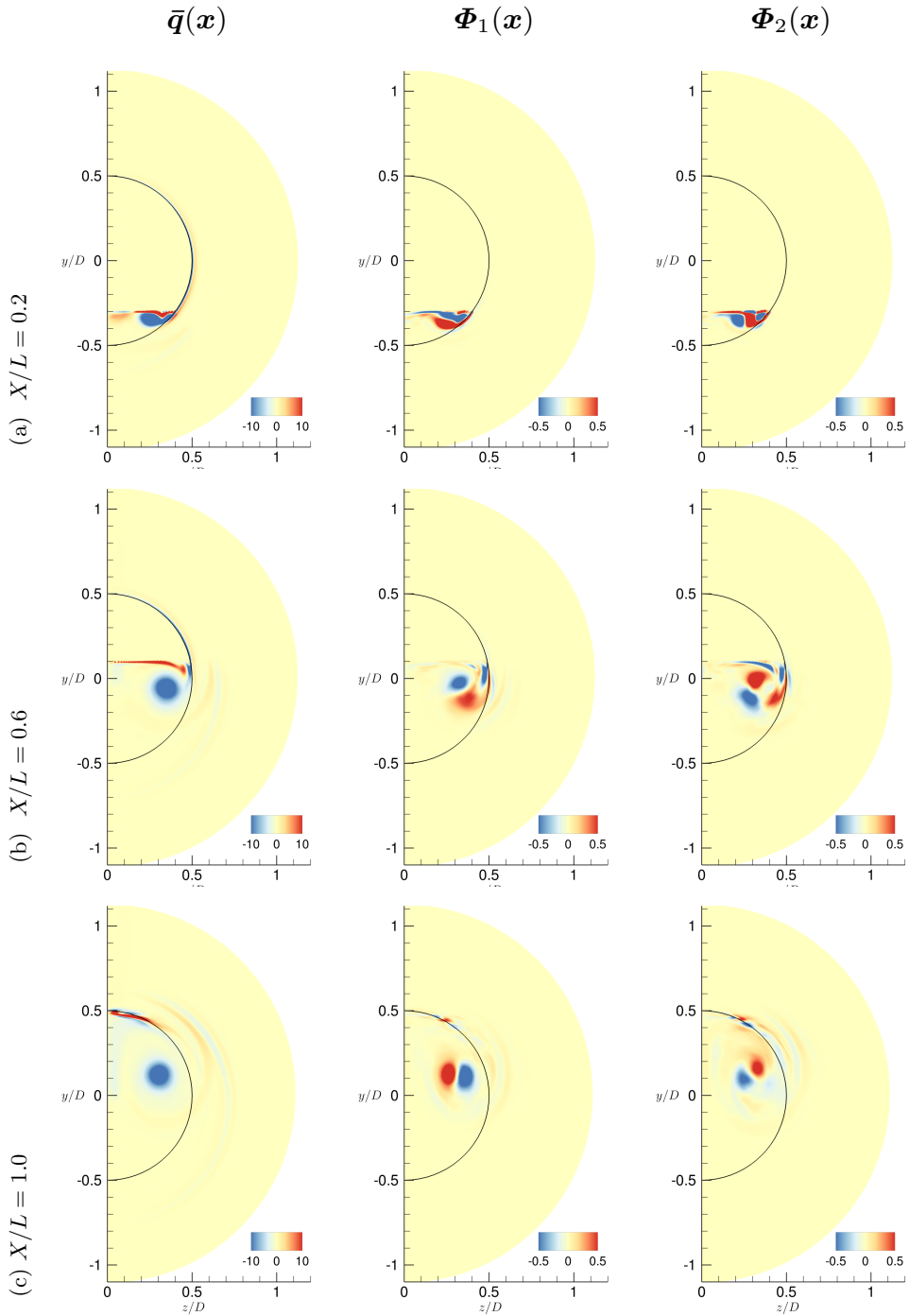


Figure 10: From left to right, mean flow as well as first two most energetic POD modes are shown through streamwise vorticity at different locations within ramp. Semi-circle indicates the boundary of the cylinder body.

have become nearly axisymmetric, but are still attached to the surfaces, both POD modes display a vortex dipole-like structure around the time-averaged vortex. However, the presence of a shear layer in the POD modes effectively diffuses these structures. Further downstream, towards the edge of the base, at $X/L = 1.0$ in figure 10(c), the vortex dipoles are clearly discernible near the vortex core for both POD modes. Smaller structures near the periphery of the cylinder display the shear layer emanating from the top. The influence of the shear layer on the vortex persists for some distance in the wake, complicating the flow dynamics.

In order to isolate the vortex dynamics and the role of large-scale coherent structures in the overall meandering process, detailed analysis is performed at a location relatively far downstream, $X/L = 2.0$. Since the instantaneous meandering motions of the two vortices in the pair are very different, as shown in figure 8, the vortices are considered separately for this component of the analysis. Figure 11(a) and (b) show the spatial structures of the first two POD modes as obtained from a decomposition of the **L** and **R** vortices separately and then plotting them together. The vortex dipoles are more distinctly defined compared to those observed at $X/L = 1.0$ in figure 10(c), while the shear layer component is very small.

The energies (Λ_i) of the first 20 most energetic modes are shown in figure 11(c,d) for the **L** and **R** vortex respectively. Both vortices show similar energy distribution among the modes. The first mode has nearly double the energy of the second, but together, these two modes contain almost 35% of the total energy. Furthermore, 80% of the flow field can be reconstructed by only considering the first 10 modes. Although first two modes differ in energy content, they may together be considered as paired helical modes with azimuthal wave number ($|m| = 1$), as in the Batchelor vortex results of Edstrand *et al.* (2016).

The movement of each vortex core in the plane depends on the alignment of the vortex dipoles compared to the mean vortex as illustrated in figure 12. The inclination angles of vortex dipoles in the first and second POD modes are defined as α_1 and α_2 , as shown in the figure, and double-sided arrows depict the oscillation axis of vortex core due to these individual dipoles. The dipole increases the vorticity in one half of the time-averaged vortex while decreasing it in the other half, thus causing the displacement, which is governed by the inclination of the dipole. In the simulation, α_1 and α_2 are approximately 16° and 106° for the left vortex, while for the right vortex, they are -16° and -106° suggesting that the coherent structures are also symmetric to each other. A 90° difference between the inclination angles, $|\alpha_1 - \alpha_2|$, for both vortices, confirm that these modes are orthogonal to each other.

The temporal dynamics of these modes are examined in figures 11(e) and (f), by considering the power spectral density (PSD) of the **L** and **R** vortices respectively. Modes for both the vortices show spectral energies largely distributed in $St_D \in [0.3 \ 2.0]$ as also observed in the analysis of point probe data (figure 9(b)). The first POD mode for both the vortices show a peak at $St_D \simeq 1.0$, while the second POD mode has more spectral energy at low-frequencies. Because of the difference in energies (Λ) of the two modes in flow, the overall motion of the vortex core is seemingly random as shown in Fig. 8. However, the high energy content of leading modes in the flow can be exploited to reconstruct meandering phenomena using a low-rank model as presented in section 7.

6. Linear Stability Analysis

Linear stability analysis is now employed to provide insights into the physical mechanism of meandering by extracting the underlying modal structures, frequencies and

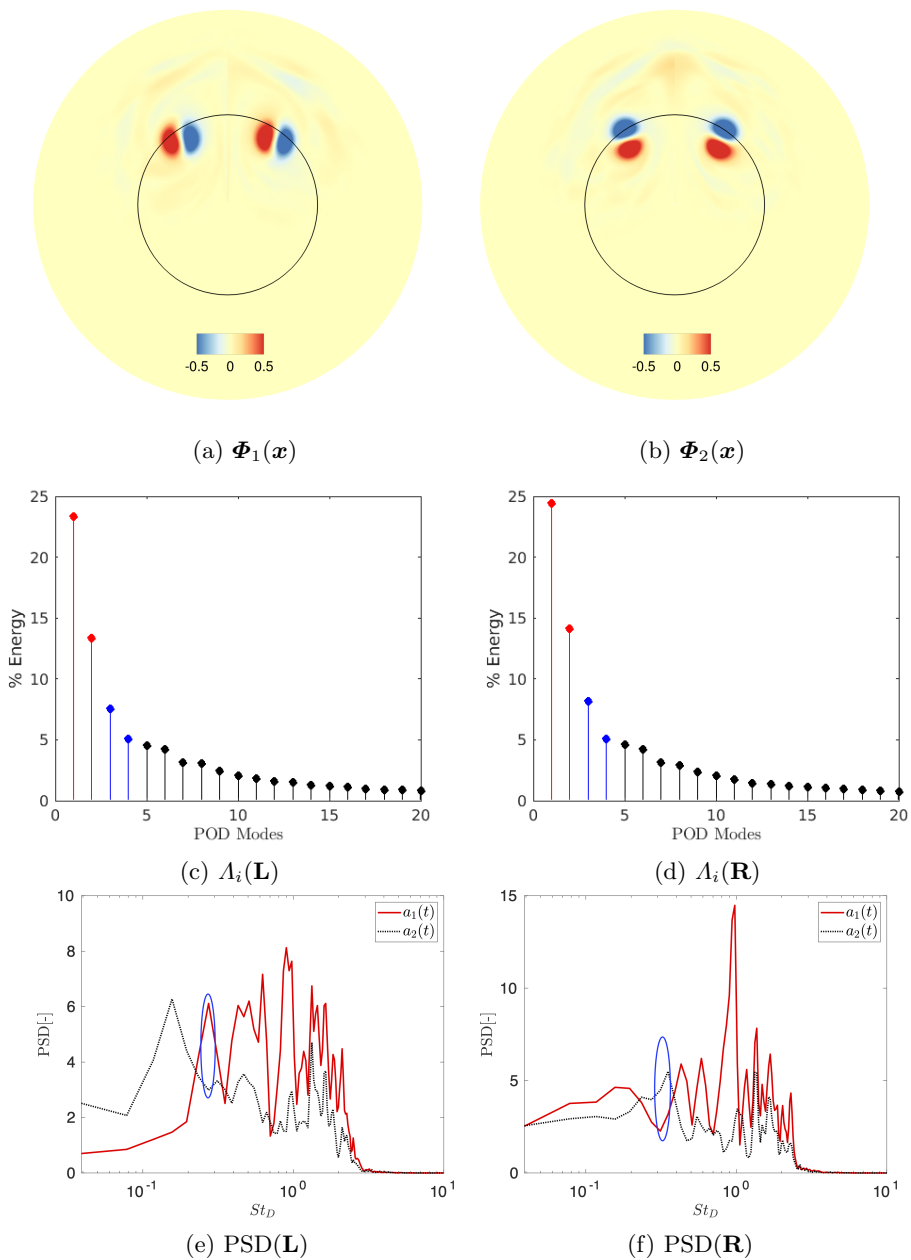


Figure 11: Dominant two POD modes at $X/L = 2.0$. Structures of mode 1(a) and 2(b). Energy content in dominant modes for \mathbf{L} and \mathbf{R} vortices (c,d). The spectral content of time-coefficients in first two modes for both the vortices (e,f). Blue ovals in (e,f) highlight the peaks around $St_D \simeq 0.3$, which are later obtained from stability analysis (section 6.3) as being associated with unstable modes.

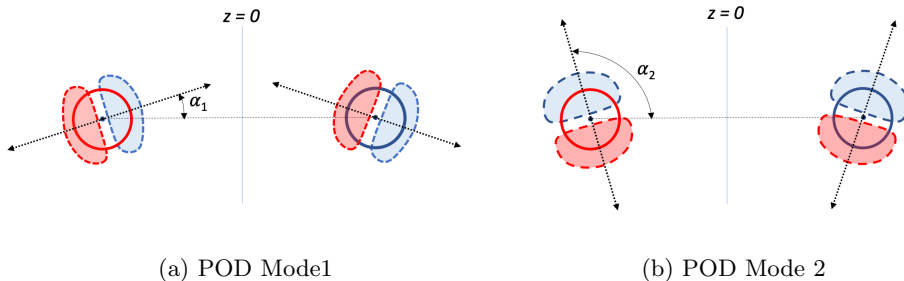


Figure 12: Sketch depicting spatial displacement of vortex cores due to the leading POD modes.

wavenumbers that form the basis for the observed phenomena. Jacquin *et al.* (2001) have observed that the cooperative interactions between the vortices affect the similar frequency range as meandering. Two typical instabilities of interest due to the mutual induction between counter-rotating vortex pairs are those designated elliptic and Crow. The former is of short-wavelength and incurs an internal deformation of the vortex cores with a wavy displacement of the vortex center (Widnall *et al.* 1971; Tsai & Widnall 1976; Sipp & Jacquin 2003). This instability thus can be viewed as a resonance between two normal modes of a vortex and an external strain field induced by the neighboring vortex. The Crow instability (Crow 1970), on the other hand, is three-dimensional, in which perturbations displace the vortices locally as a whole without any change in their core structure; the observed wavelengths are large compared to the core radius. This instability can be observed in aircraft tip vortices (Lewke & Williamson 1998).

A rough estimate of the features of these instabilities, if present, can be obtained by considering the characteristic length scales in the vortex pair, namely the core radius δ and the inter-vortical separation b ; their ratio, δ/b , indicates the relative distance between the vortices. Values obtained in the current simulations, reported in Table 1, are consistently between 0.1 and 0.2 at all streamwise locations. According to Lewke *et al.* (2016), these lie in the range that can trigger both long and short wave instabilities, though Reynolds number considerations are also important.

The instabilities existing in the flowfield are now investigated in detail through a linear stability analysis. The mean vortex pair is first matched to a theoretical vortex model, and both temporal and spatial stability analyses are performed. Analyzing a fitted model vortex is advantageous because it offers the flexibility to extend the domain arbitrarily without compromising effects due to boundaries. This also facilitates the examination of the long-wavelength Crow instability, if present. The possibility of a global mode is not examined as it is beyond the scope of the present study. Parallel flow is assumed in the streamwise direction; this is a reasonable assumption since the streamwise variation of the mean flow is relatively small at distances sufficiently downstream of the body such as those considered here. As such, stability characteristics of the vortices predicted with parallel flow assumption provide a reasonable description of the meandering phenomena (Edstrand *et al.* 2018).

6.1. Theoretical Vortex Model

Afterbody vortices, such as the ones of interest, are characterized by two components: swirl and strain. While the swirl effect is accounted through the radially varying in-plane velocity field, the axial velocity provides the strain field. The mean vortical field at location $X/L = 2.0$ was shown earlier in figure 4, while the mean axial velocity

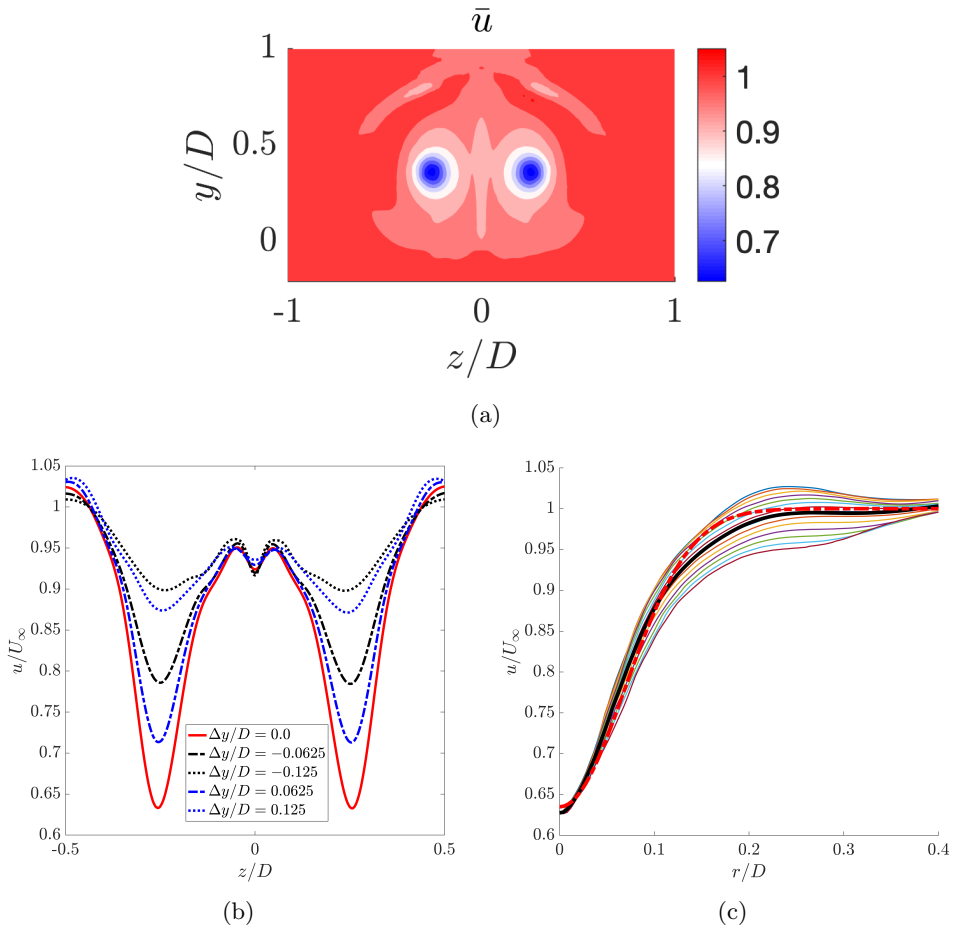


Figure 13: Axial velocity distribution at a streamwise location $X/L = 2.0$. (a) \bar{u} contours. (b) Wake-like behavior shown by velocity distributions at different vertical locations measured from the vortex center. (c) Fitting of axial velocity from simulations to the Batchelor vortex. The thick black line indicates the azimuthally averaged axial velocity, and the red dashed line indicates the axial velocity in the fitted Batchelor vortex. Note the vortex in the simulation is recentered at $(0,0)$ after interpolating to the cylindrical coordinate system.

distribution in the vortex is shown in figure 13(a). As expected, the velocity is minimum at the center of the vortex and increases along the radial direction, eventually reaching free-stream values about 10 core radii (δ) away from the center. The quantitative profiles in figure 13(b) at different vertical locations show typical wake-like behavior. An important point to note is that the magnitude of \bar{u} never reaches the free-stream value between the vortices because of their relatively close proximity to each other. This motivates the use of a vortex pair as opposed to an isolated \mathbf{L} or \mathbf{R} vortex for the present analysis.

Wake vortices have been modeled with different theoretical models that contain their characteristic information. Vortex models used in the literature for analyses of wingtip or similar vortices include the Batchelor or q -vortex (Edstrand *et al.* 2016), Lamb-Oseen vortex (Antkowiak & Brancher 2004), Lamb–Chaplygin vortex (Jugier *et al.* 2020),

Rankine vortex (Lacaze *et al.* 2005) and Moore-Saffman vortex model (Feys & Maslowe 2016). Among these, the Batchelor and Moore-Saffman models account for axial flow and hence are more realistic in providing the dynamics of interest in this work. We employ the Batchelor model to match the individual vortex in the current streamwise vortex pair as the role of the axial velocity in the stability mechanism may be crucial. Although this model vortex is typically expressed in cylindrical coordinates, we analyze them in the Cartesian system to account for the two vortices in the pair. In this system, the velocity components for the Batchelor vortex can be written as (Paredes *et al.* 2011):

$$u = 1 - \gamma(x) \exp\left(\frac{-r^2}{\delta(x)^2}\right) \quad (6.1a)$$

$$v = -\frac{\kappa}{r^2}(z - z_0) \left(1 - \exp\left(\frac{-r^2}{\delta(x)^2}\right)\right) \quad (6.1b)$$

$$w = \frac{\kappa}{r^2}(y - y_0) \left(1 - \exp\left(\frac{-r^2}{\delta(x)^2}\right)\right) \quad (6.1c)$$

where (y_0, z_0) is the center of the vortex and $r^2 = (y - y_0)^2 + (z - z_0)^2$. The quantity $\delta(x)$ corresponds physically to the dimensionless local vortex core radius. $\gamma(x)$ is the axial velocity defect and κ is a swirl strength parameter.

For the current analysis, one vortex is first matched to the model, and the other anti-symmetric vortex is then placed at the separation distance b . The simulation results are first interpolated on a cylindrical grid and the axial velocity u is then azimuthally averaged to obtain the parameters for the fitted Batchelor vortex. Edstrand *et al.* (2016) have found that stability results are insensitive to the averaging process. Figure 13(c) shows the radial variation of axial velocity at different azimuthal locations. The azimuthally averaged vortex velocity as well as the fitted Batchelor vortex model are also shown.

Figure 14 compares the velocity fields in mean \mathbf{R} -vortex obtained directly from simulations with those of the fitted vortex used for stability analysis. All the three velocity components considered in the model show good match with the LES data. The parameters of this matched Batchelor vortex are $\delta = 0.0972$, $\gamma = 0.365$, $\kappa = 0.07$, to obtain a non-dimensional swirl parameter $q = \kappa/(\delta\gamma) = 1.9731$. This value of q is much smaller than the $q = 4.41$ obtained for trailing edge vortex in Edstrand *et al.* (2016). The present parameters correspond to a Reynolds number based on the core radius as $Re_\delta \equiv U_\infty\delta/\nu \simeq 2500$, which is much lower compared to $Re_\delta = 27,200$ used in the stability study of wingtip vortices (Edstrand *et al.* 2016).

6.2. Stability Approach

Most stability studies in the literature consider an isolated vortex and efforts on vortex pairs separated by a relatively small distance, and in the presence of an axial flow, are relatively rare. The latter problem presents substantial computational challenges as the domain becomes significantly larger (Hein & Theofilis 2004). To ease the computational burden, temporal stability analyses are performed for a given wavenumber range while spatial analysis at the most unstable frequency is used to further confirm the results. Further, incompressible linearized Navier-Stokes equations are considered for the eigenvalue analysis instead of compressible equations as the latter increases the linear operator size significantly due to an extra variable. This is acceptable because of the low Mach regime considered and a comparison with the fully compressible formulation is given below to ensure confidence. Consistent with the simulations, a spanwise coordinate system is used in which two inhomogeneous spatial directions, y and z , are resolved simultaneously, while

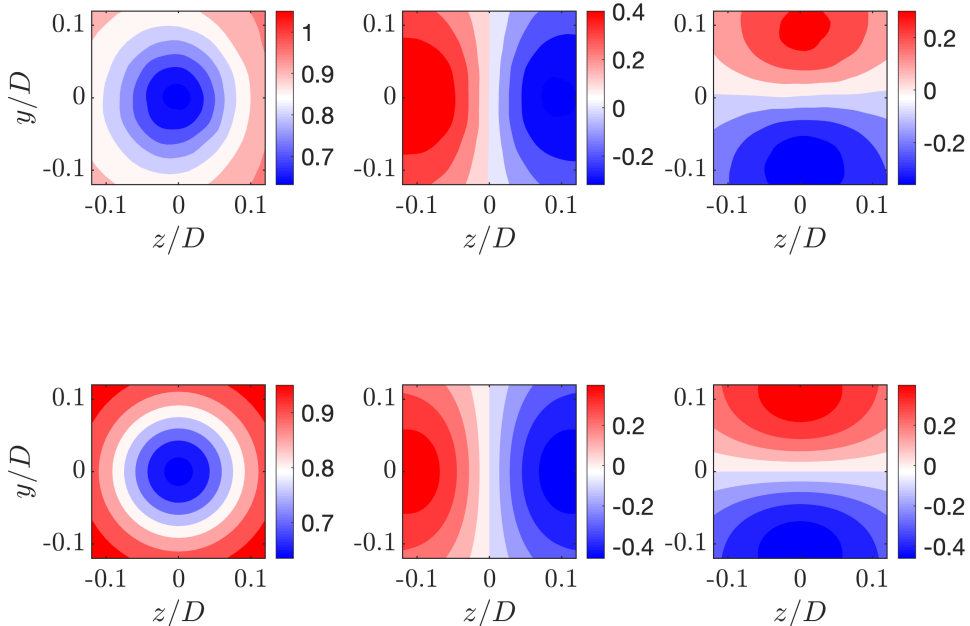


Figure 14: Top: \mathbf{R} -vortex from the simulation. Bottom: Theoretical Model (Batchelor vortex). U, V, W velocity components are shown from left to right. Note the \mathbf{R} -vortex in simulation is centered to $(0,0)$ to compare with the fitted Batchelor vortex.

the axial direction, x , is considered to be locally homogeneous. The resulting eigenvalue problems along with boundary conditions for both temporal and spatial analyses are summarized in appendix A.

Hein & Theofilis (2004); González *et al.* (2008) have described the importance of choosing a sufficiently large domain for solving the eigenvalue problem, and a suitable grid discretization scheme to resolve the vortex core and wake regions adequately, while ensuring proper treatment of the relatively innocuous farfield. Because of the large domain, whose size scales as $y_\infty/\delta \approx 20$, $z_\infty/\delta \approx 20$ (Edstrand *et al.* 2018; Hein & Theofilis 2004; Paredes *et al.* 2011), finite difference schemes are not generally a preferred choice because of the large number of grid points required in the farfield region. Hein & Theofilis (2004) use a mapping ζ of Chebyshev collocation points $\eta_j \in [-1; 1]$ such that:

$$\zeta_j = \zeta_\infty \frac{\tan \frac{c\pi}{2} \eta_j}{\tan \frac{c\pi}{2}} \quad (6.2)$$

where ζ_∞ is the farfield boundary. The stretching parameter $c \in (0, 1]$ defines the clustering of grid points near the vortex core. Higher c provides more clustering near the vortex core while imposing a relatively coarser grid away from the core. This distribution of points will be referred to as the CHEB-TANH grid. Figure 15(a) shows a typical grid clustering for $\delta = 1$, $y/\delta \in [-20; 20]$, $z/\delta \in [-20; 20]$, $N_y = N_z = 72$, $c = 0.975$, ensuring that the vortex at the center is adequately resolved.

For a vortex pair, the choice of discretization scheme requires more care than for a single vortex, because of their separation along the z -axis connecting their centers. The domain used for the two vortex system is $y/\delta \in [-20; 20]$, $z/\delta \in [-20 - b/2; 20 + b/2]$, where b is the separation between vortices as defined earlier. Naturally, for similar accuracy, the number of grid points required is much higher than the single vortex case, as the

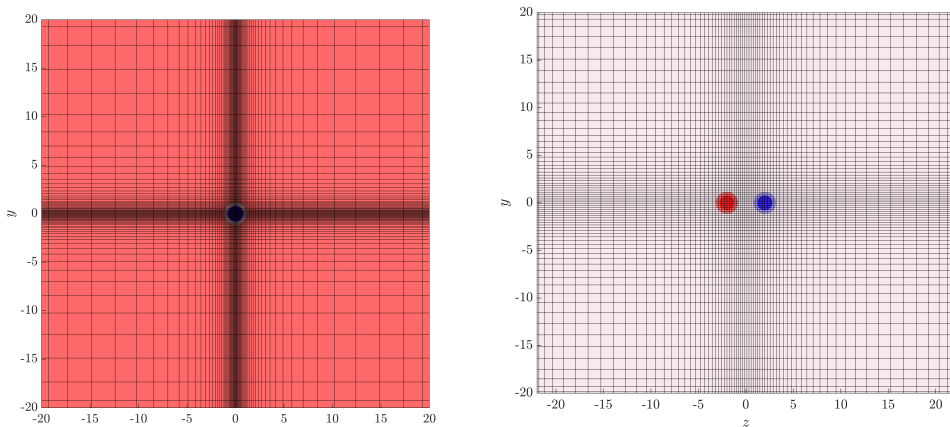
(a) Isolated vortex (72×72 , $c = 0.975$).(b) Vortex pair (100×100 , $c = 0.75$).

Figure 15: Spatial discretization for stability analysis.

stretching parameter, c , in the CHEB-TANH needs to be relaxed to encompass both the vortices. Figure 15(b) shows a representative grid clustering for $c = 0.75$, resolving both the vortices as well as the spacing between them.

Table 2 shows validations for both temporal and spatial stability codes used in the study. For the temporal approach, the classical q -vortex at $q = 0.475$, $Re = 100$, $k = 0.418$ is chosen; this problem was first examined by Mayer & Powell (1992) and subsequently used for validation in several studies (Hein & Theofilis 2004; Paredes *et al.* 2011; Edstrand *et al.* 2018). The results for the unstable mode are reported along with the reference results from Paredes *et al.* (2011). Excellent convergence is obtained with the mapped CHEB-TANH discretization, even for a slightly smaller domain in $[-15, 15]$ and moderate grid size. The stretching parameter in this discretization is fixed at $c = 0.975$, ensuring that the vortex at the center is adequately resolved. A good match is also obtained with the sixth-order finite difference (FD6) approach albeit at a higher resolution. The table also includes a result when a fully compressible stability solver is used for the same q -vortex analysis at a low Mach number ($M = 0.1$). Comparing the results between incompressible and compressible solvers with similar grid and numerical schemes, we note only a minor difference of about 1% in the frequency and 0.44% in the growth rate.

For the spatial code validation, the Batchelor vortex study by Paredes (2014) at $\kappa = 0.8$, $\gamma = 0.8$, $\delta = 1$, $Re = 3000$ is used for reference. In table 2, results for $m = 1$, $\omega = 0.86$ are compared against the values reported in Paredes (2014). Even with a moderate 40×40 grid, the frequency obtained in the current study is within 2% of the reported value; the comparison improves with increase in grid size. For the subsequent results for current afterbody vortices, CHEB-TANH grid is employed.

6.3. Stability Analysis of Afterbody Vortices

The stability dynamics of the afterbody vortices are now delineated. Before showing the dynamics of the vortex pair, we first discuss the stability characteristics of an isolated vortex. The fitted Batchelor vortex described in section 6.1 is used for this study. Figure 16(a) shows results from spatial analyses of this vortex for input frequency

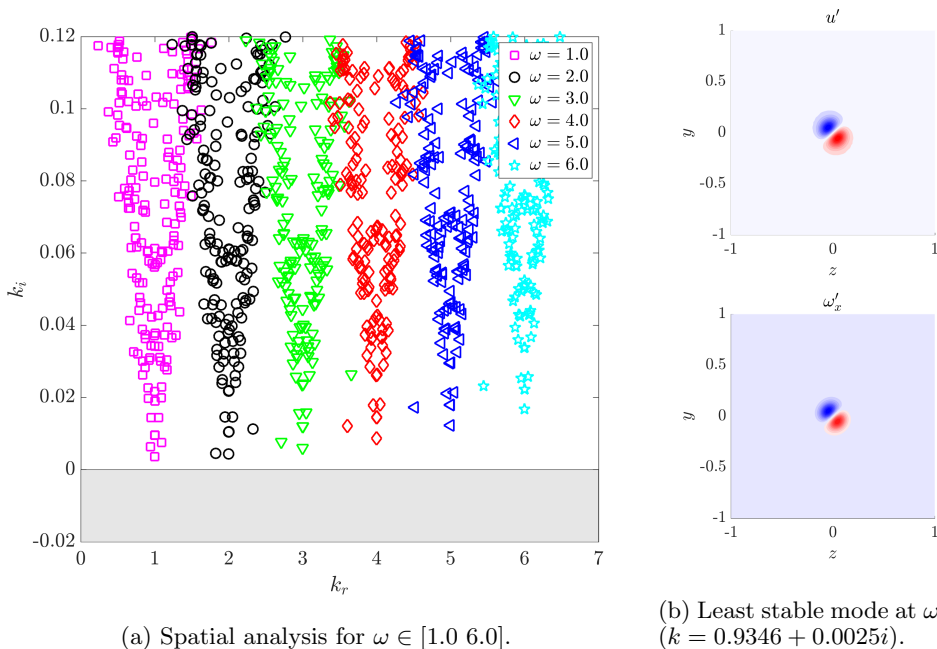
Domain	Diff. Scheme	Resolution	Temporal	Spatial
Paredes	FD10		0.028353+0.009617i	0.543-0.185i
[-15 15]	CHEB-TANH	40 × 40	0.028337 + 0.009607i	0.5534-0.1839i
[-20 20]	CHEB-TANH	60 × 60	0.0283321 + 0.0096043i	0.549-0.18i
[-15 15]	FD6	101 × 101	0.028533 + 0.009980 i	
[-15 15]	FD6(C)	101 × 101	0.028225 + 0.010024 i	

Table 2: Validation of stability analyses techniques. The temporal analysis is performed for a q -vortex with parameters $q = 0.475$, $Re = 100$, $k = 0.418$. The spatial analysis is performed for the Batchelor vortex ($\kappa = 0.8$, $\gamma = 0.8$, $\delta = 1$) at $\omega = 0.86$ and $Re = 3000$. Temporal analysis using compressible formulation, FD6(C), at low Mach number ($M = 0.1$) yields leading modes close to those obtained with fully incompressible code.

varying from $\omega = 1$ to $\omega = 6$. A 60×60 grid with $c = 0.975$ is used for these analyses. As seen from the figure, the vortex is stable for the entire frequency range $\omega \in [1.0 \ 6.0]$. The vortex becomes increasingly more stable as the frequency is increased. For input frequency $\omega = 1$, the least stable mode is obtained at $k \equiv k_r + ik_i = 0.9346 + 0.0025i$. Note that the positive value of k_i in the spatial analysis indicates a decaying mode (see appendix A). The spatial structure of this mode is shown in Fig. 16(b). Both the axial velocity and vorticity fluctuations show dipole structures indicating the $|m| = 1$ elliptic mode discussed earlier. This mode is typically observed to be the dominant instability mechanism in wake vortices (Edstrand *et al.* 2016).

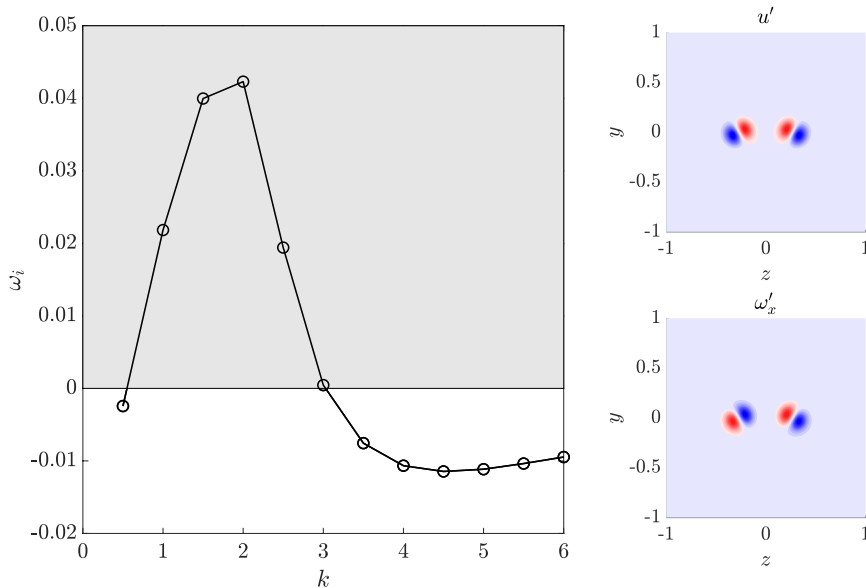
Now we consider the change in stability characteristics due to the presence of a counter-rotating vortex next to the above stable vortex. Following the results of Section 4, the counter-rotating vortices are separated by $b/\delta = 5.6132$. As alluded to earlier, this relatively large separation between the vortices increases the computational requirement enormously because the stretching parameter needs to be relaxed to as low as 0.75, with a corresponding increase in the grid size to ensure sufficient accuracy. The parallel spatial analysis, performed above for the isolated vortex, is natural for the study of the vortex pair also, since it directly provides the wavenumber at which the flow can become unstable. However, since the grid size required for vortex pair is significantly larger (up to 150×150) than that for an isolated vortex, we use a temporal approach with wavenumber variation to extract the least stable wavenumber.

The temporal analysis results for a streamwise wavenumber sweep of $k \in [0.5 \ 6.0]$ is shown in Fig. 17(a). These results are obtained by using a 140×140 CHEB-TANH grid that gives a dense matrix of $78,400 \times 78,400$. The vortex pair displays unstable eigenmodes at wavenumbers $1.0 \leq k \leq 3.0$, with growth rate increasing between $k = 1.0$ and $k = 2.0$. As the input wavenumber increases beyond $k = 2.0$, the modes become less unstable and only stable modes are recovered for $k > 3.0$. For the subsequent analyses, we focus on the wavenumber $k = 2.0$ at which the fastest growing modes are recovered. Figure 18(a) shows the convergence of dominant modes in the eigenspectrum at this wavenumber as obtained by performing the analysis on a finer 150×150 grid. Both grids recover most unstable modes at $\omega \equiv \omega_r + i\omega_i = \pm 1.988 + 0.0417i$ (note only the positive frequency ω_r mode is shown). The phase speed of this mode is $c_r \equiv \omega_r/k = 0.9940$. In order to confirm that spatial analysis also recovers similar instabilities, we show the eigenspectrum from this approach at input frequency $\omega = 2.0$ in figure 18(b). Note that the matrix size for the spatial problem is very large ($137,200 \times 137,200$) for a similar grid size of


 (a) Spatial analysis for $\omega \in [1.0 \ 6.0]$.

 (b) Least stable mode at $\omega = 1$
 ($k = 0.9346 + 0.0025i$).

Figure 16: Eigenspectrum from spatial analyses of an isolated vortex for a range of frequencies(a). Shaded portion indicates the region of growing modes ($k_i < 0$). The least stable mode at $\omega = 1$ shows $m = 1$ elliptic instability (b).


 (a) Temporal analysis for $k \in [0.0 \ 6.0]$.

 (b) Unstable mode at $k = 2$.

Figure 17: Eigenspectra from temporal analyses of the vortex pair for a range of wavenumbers (a). Shaded portion indicate the region of growing modes ($\omega_i > 0$). Structure of the fastest growing mode at all wavenumbers is shown in (b).

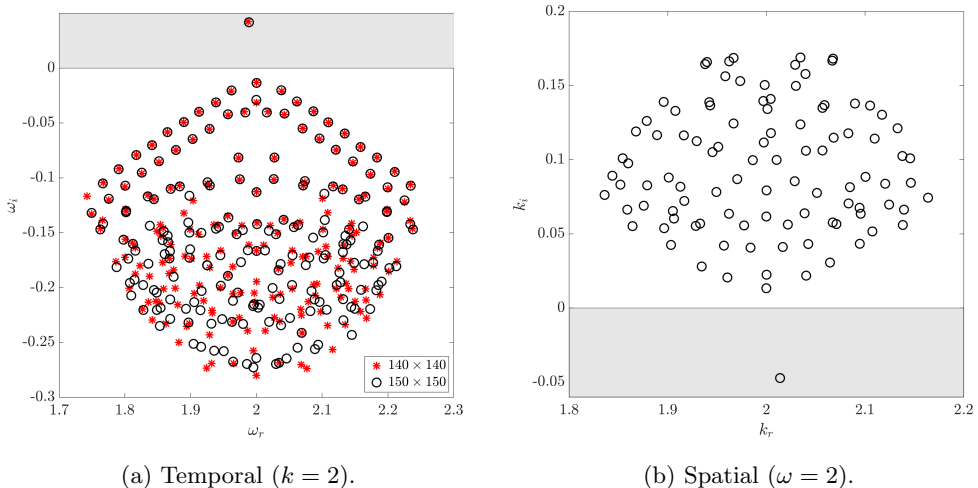


Figure 18: Eigenspectra from temporal(a) and spatial(b) analyses of the afterbody vortex pair. Both approaches show analogous instabilities at a phase speed of about 0.99.

140×140 and solving this eigenvalue problem with a Krylov size of 100, requires about 140 gigabytes of the physical system memory. The spatial analysis recovers an unstable mode at $k \equiv k_r + ik_i = \pm 2.0138 - 0.0473i$ as shown in the unstable region ($k_i < 0$) in figure 18(b). The phase speed of this mode, $c_r \equiv \omega/k_r = 0.9932$, is very similar to that obtained from the temporal analysis earlier. The recovery of analogous instabilities in both spatial and temporal approaches further validates present observations.

The structure of this mode as obtained from both temporal and spatial approaches is very similar as shown in figure 17(b). The shape exhibits a dipole form representing the $|m| = 1$ elliptic mode for both vortices in the pair, as observed in POD analysis. This dipole is extracted in both the axial velocity and vorticity fluctuations, but it is symmetric about the mid-plane ($z = 0$) in the former, but anti-symmetric in the latter. This is consistent with the symmetry of the mean flow. The inclination of the dipole with respect to the horizontal axis, α_1 (see sketch 12), is about 30° , which is higher than that observed in POD mode 1. This suggests that the interaction of the downstream shear layer with the vortices, as well as non-linearities present in the flow, modifies these structures and introduces high-frequency content as evident in the spectral signatures of the POD modes (figure 11(e,f)).

The frequency of the most unstable mode as obtained from the temporal analysis is $\omega \simeq 1.988$, or equivalently $St_D \simeq 0.32$. This low-frequency was observed in the vortex flowfield (figure 9(b)) as well as in the POD modes (figure 11(e,f)). As mentioned earlier, in the experimental work of ZGUNOV *et al.* (2020a) this low-frequency was observed and was conjectured to be related to fluctuations due to interactions of cores. The present stability analysis confirms this hypothesis and establishes meandering as a low-frequency phenomenon in afterbody flows in similarity with vortices in aircraft wakes (Jacquin *et al.* 2001).

To further confirm the role of the interaction between the vortices as a necessary mechanism for the recovery of unstable modes, we perform the temporal stability analysis for an isolated vortex with the same swirl and strain as in each individual vortex in the pair. Figure 19(a) shows the result from this analysis along with grid convergence for the dominant modes as obtained with two grids. Unlike in the two-vortex system,

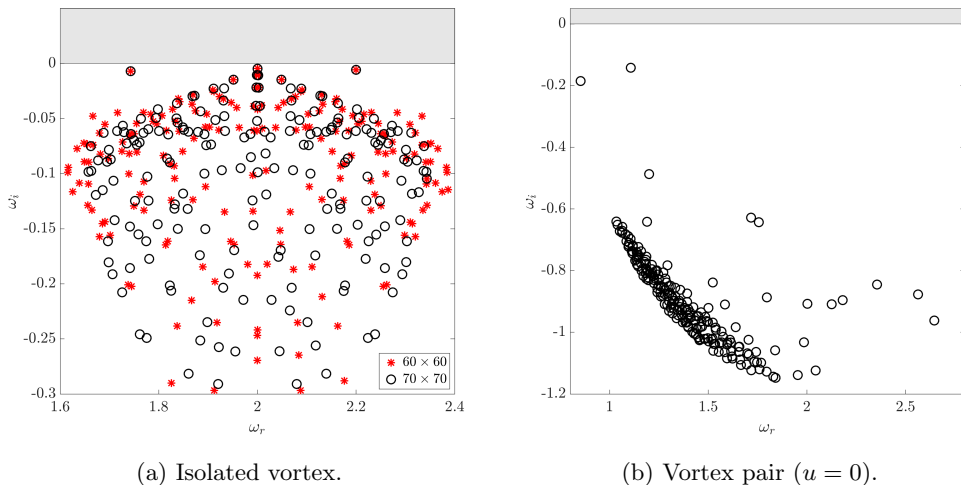


Figure 19: Eigenspectra from temporal analysis at $k = 2.0$. (a) Isolated vortex with axial velocity. (b) Vortex pair with no axial velocity.

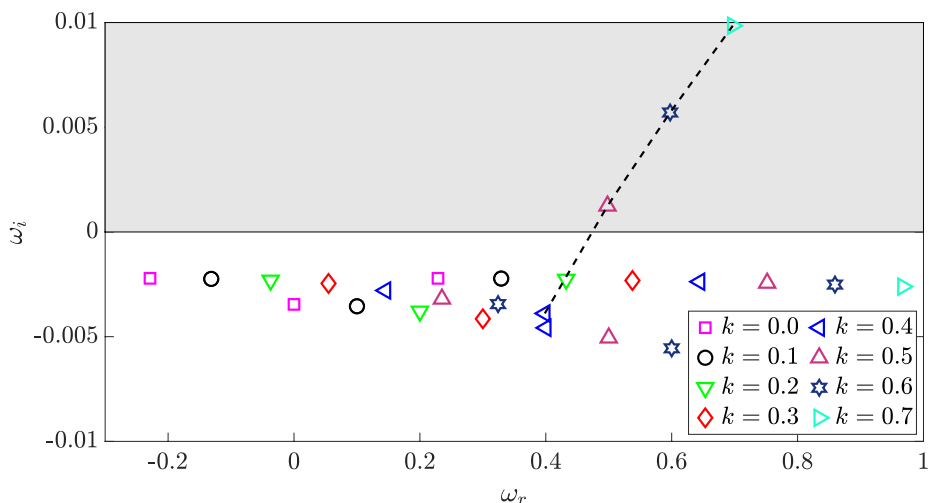


Figure 20: Eigenspectra from temporal analyses of the afterbody vortex pair at low wavenumbers. No unstable modes are recovered below $k = 0.5$.

all modes recovered in this analysis are decaying. The least stable modes are found at $\omega = \pm 2.0001 - 0.0047i$ exhibiting dipole structures for both vorticity and axial velocity, which is similar to that shown in figure 16(b).

The external strain field is influenced by the neighboring vortex, and is accounted for in the stability calculations through the axial velocity component. The correlation analysis of section 5.1, based on the phenomenological description of instantaneous vortex cores on a sectional plane, indicates only weak influence of the vortices on one another. That analysis, however, did not include the axial velocity component, whose role in destabilizing the vortices is now clarified. A stable vortex can become unstable even without the presence of axial flow (as in the Kelvin vortex) due to an elliptic instability

of the core; however, the presence of an axial flow can make an otherwise stable vortex unstable (Lacaze *et al.* 2005; Jacquin *et al.* 2005). In order to examine the effects of this strain, the temporal stability analysis was repeated on the afterbody vortex pair by setting the axial velocity to zero. The problem then becomes essentially similar to Rankine vortex models used in the literature to study elliptic instabilities (Kerswell 2002). The eigenspectrum thus obtained is shown in figure 19(b). A key observation is that unlike the analysis with the axial velocity (figure 18(a)), no unstable mode is recovered in this calculation. Further, the modes are far removed from the zero axis. Although not shown, the shapes of dominant modes continue to show helical structures. The present analysis thus shows that it is necessary to consider a vortex model that includes the strain field in order to recover the correct instability behavior in afterbody vortices.

Finally, the possible presence of long-wavelength (small k) Crow instability in the flow is briefly investigated. The least stable mode at $k = 2$ in figure 17(b) is inclined at 30° to the horizontal. The Crow instability on the other hand typically manifests a 45° inclination in the structure (Brion *et al.* 2008). To confirm this further at low wavenumbers, the temporal analysis was performed using a k -parameter sweep between 0.0 and 1.0 at increments of 0.1. Figure 20 shows the resulting eigenspectra for all these wavenumbers for the current vortex pair. No unstable mode is observed in the k -range of $[0.0 \ 0.4]$, and the first unstable mode occurs at $k = 0.5$. The growth rate of modes continues to increase with wavenumber until $k = 2.0$ as discussed earlier. This indicates the absence of the Crow instability in this flow, although simulations with a longer domain may be necessary to establish this fact numerically. Further, the flow conditions that lead to a change in the non-dimensional swirl parameter or the Reynolds number may affect this observation, as discussed in Hein & Theofilis (2004). Another key parameter in the analysis that determines the interaction between the two vortices is the separation distance, b/δ . If this distance varies substantially with the upsweep angle ϕ of the afterbody, the analysis needs to be repeated to examine the stability mechanism.

7. Low-rank Representation

The characteristics of the POD and flow stability modes discussed above indicate the potential for a low-rank unsteady vortex meandering model using POD-based coherent structures. The reconstruction using a range of modes between m_1 and m_2 , $\tilde{\mathbf{q}}_{m_1, m_2}(\mathbf{x}, t)$, may be performed using the definition of POD in equation (5.2) as:

$$\tilde{\mathbf{q}}_{m_1, m_2}(\mathbf{x}, t) = \bar{\mathbf{q}}(\mathbf{x}) + \sum_{i=m_1}^{m_2} \sqrt{\Lambda_i} \Phi_i(\mathbf{x}) \mathbf{a}_i(t) \quad (7.1)$$

The influence of POD modes 1 and 2, as described in section 5.2, is examined first by adding them individually to the mean flow and reconstructing the solution. Subsequently, the combined effect of both helical modes is examined in reproducing meandering effects. Figures 21(a,b) show the displacement of the \mathbf{R} -vortex core at $X/L = 2$ when the first two POD modes are added individually to the mean flow at a representative time. The reconstructed vortices display slightly non-axisymmetric structure due to the addition of these modes. Furthermore, the core, as estimated by the innermost black contour, is displaced from its mean position shown with a broken white contour. The displacement of the core is in the direction of the inclination of the dipoles shown earlier in figure 12. When the two modes are added, the effective displacement of the core from the mean position is shown in Figure 21(c).

The efficacy of a low-rank approximation may be evaluated by comparing the LES

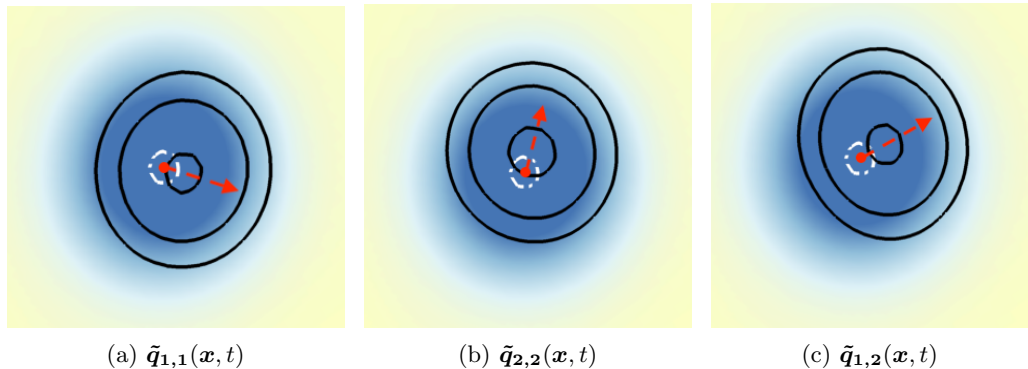


Figure 21: Displacement of mean vortex core due to most energetic POD modes. Mean \mathbf{R} -vortex ($\bar{\mathbf{q}}(\mathbf{x})$) is shown with flooded contours using the streamwise vortex at contour levels between -10 and 10 . Broken white lines indicate the core. Reconstructed vortex cores ($\tilde{\mathbf{q}}_{m_1, m_2}(\mathbf{x}, t)$) are shown in solid black lines. The red arrow shows the direction of movement of the mean vortex center due to superposition of first mode(a), second mode (b) as well as both first and second modes (c). In (a,b), the arrow directions are consistent with the alignment of modes, α_1 and α_2 in figure 12.

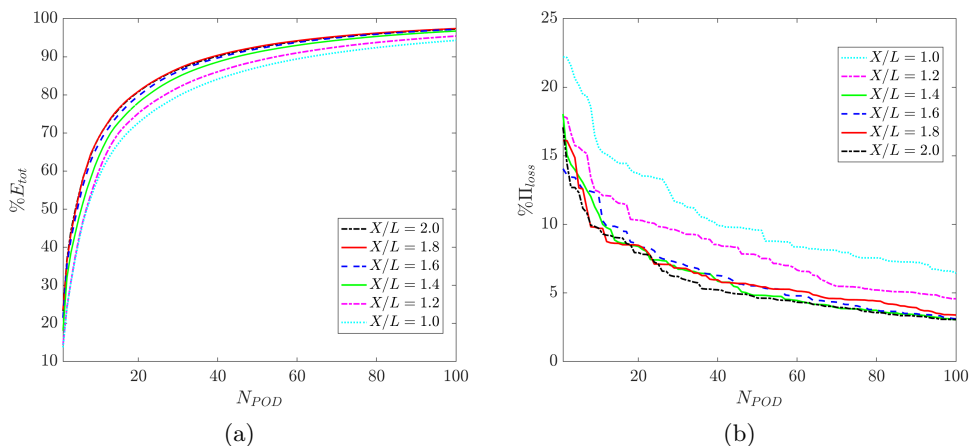


Figure 22: Comparison of energy of POD modes (a), and performance losses in reconstruction (b) at different streamwise locations.

result with reconstructed spatio-temporal evolution of the vortex cores due to a small subset of modes, taking into account the different energy content of each mode. The rank-order of the approximation is a function of the streamwise location chosen since the intensity of meandering as well as the proximity of the separating shear layer can alter the properties of the POD modes (*e.g.*, compare leading modes at $X/L = 1.0$ and 2.0 in figures 10 and 11 respectively). The cumulative energy content,

$$E_{tot} = \sum_{i=1}^{N_{POD}} A_i \quad (7.2)$$

due to N_{POD} modes is shown in figure 22(a) for six locations downstream of the body at an interval of $\frac{\Delta x}{L} = 0.2$. The total energy contribution due to dominant modes gradually

increases with the downstream distance, with nearly overlapping mode contributions for $X/L = 1.8$ and 2.0 . Comparing the situation at $X/L = 1.0$ and 2.0 , the first two modes contribute to about 24% and 37% of the total energy of flow respectively, while the first 100 modes respectively account for 97.3% and 94.3%.

The disparity in energy content of dominant modes at different locations is expected to affect the reconstruction of flowfields with these modes. Figure 23 compares the actual and reconstructed flowfields at three locations when 2, 10 and 100 modes are considered respectively. At the primary location of interest, $X/L = 2.0$ in Fig. 23(a), a reasonable description of the streamwise vortices is obtained with only the first two modes. These modes also contribute to the large-scale structures in the top shear layer away from the vortices. The next 8 modes primarily contribute to small-scale structures surrounding the vortices and the top shear-layer. When 100 of the total 3,000 modes are used for reconstruction, the structure is very similar, qualitatively and quantitatively, to the LES result.

At locations closer to the body, $X/L = 1.4$ and 1.0 , shown in Fig. 23(b) and (c) respectively, the first two modes contribute to the coherent structures of the vortices. However, due to high meandering intensity at these locations, the structures of the reconstructed vortices are significantly different from the LES snapshots. The addition of more modes improves the result as expected, with about 100 modes nearly reconstructing the complete flowfield with reasonable accuracy.

A performance loss parameter Π_{loss} is used to quantify the error in reconstruction, similar to that used in Jovanović *et al.* (2014):

$$\Pi_{loss} = \frac{\|\mathbf{q} - \tilde{\mathbf{q}}\|_2}{\|\mathbf{q}\|_2} \quad (7.3)$$

Figure 22(b) displays these losses at six locations between $X/L = 1.0$ and 2.0 . Even with only one POD mode, the maximum performance error is only 23% across all locations, further confirming the low-rank behavior of the flow. As expected, the losses are higher at locations near the body, with a difference of about 5% between $X/L = 1.0$ and 1.2 . Away from the body, for example at $X/L = 2.0$, the loss is about 3% with 100 modes. At $X/L = 1.0$, this loss is slightly higher (8%). Further, as described above in the context of Fig. 23(a), the major factor contributing to error observations at the farthest location ($X/L = 2.0$) is the absence of finer structures in the first few modes; two modes by themselves recreate the streamwise vortices reasonably well.

The effects of low-rank approximation on the temporal dynamics at this location are now compared to the meandering observed in the LES field. As explained earlier, the reconstruction results in vortex motion that does not follow a preferred displacement direction but rather moves around in a manner that represents the meandering observed in the LES. The temporal displacement of the vortex cores at $X/L = 2.0$, when the effects of the leading modes are added are shown in figure 24 for the **L** vortex. The individual displacement due to the first and second modes considered separately are depicted in figures 24(a) and (b), respectively for 100 time-steps. These figures confirm that the motions of the core induced by mode 1 and 2, by themselves, lie along straight lines. The slopes of these lines, α_1 and α_2 , are consistent with the structures of the vortex dipoles as described earlier in § 5.2.

Although the displacements due to the individual modes are relatively simple, their combined effect is not. The trajectory of vortex cores due to both modes, shown in figure 24(c), are clearly very complex and are established due to the combination of two nearly straight lines in an effect similar to Lissajous curves (Fahy & Karioris 1952) generated by a system of parametric equations. The combined displacement due to both these modes

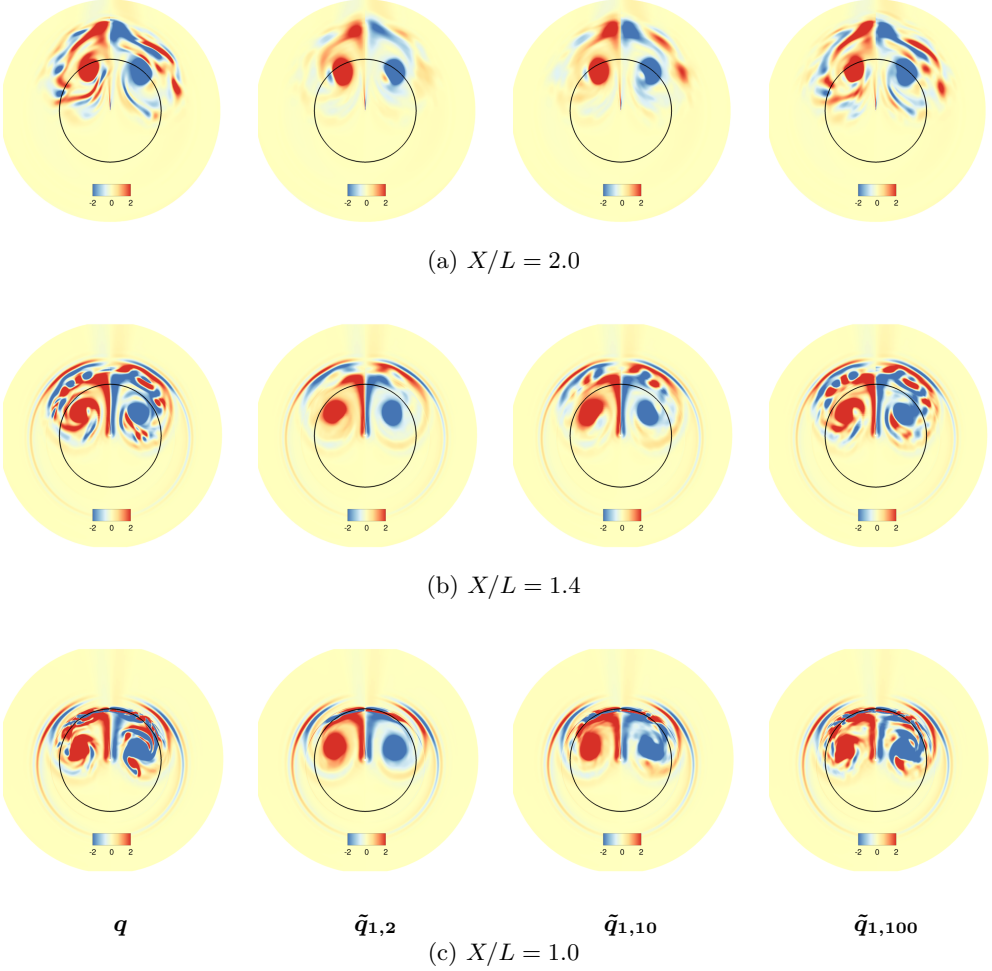


Figure 23: Reconstruction of flow fields using POD modes. The first two modes are major contributors to the coherent structures of the streamwise vortices. At locations closer to the body e.g., at $X/L = 1.0$ and $X/L = 1.4$, the meandering intensities are higher and therefore reconstructed vortices with just two modes differ significantly from the LES. In all three cases, 100 of the total 3,000 modes reconstruct the complete flowfield to reasonable accuracy.

may be compared with the actual meandering motion shown in figure 24(f). Even when only the two dominant POD modes are considered, the result qualitatively reproduces the complex clockwise movement of the core, although the maximum displacement of core in the reconstructed flowfield is smaller than the original flowfield. The error in reconstruction may be characterized using the displacement from the vortex location in the root-mean-square sense as:

$$E_d = \sqrt{\frac{\sum_{i=1}^N ((y_i - \tilde{y}_i)^2 + (z_i - \tilde{z}_i)^2)}{N}} \quad (7.4)$$

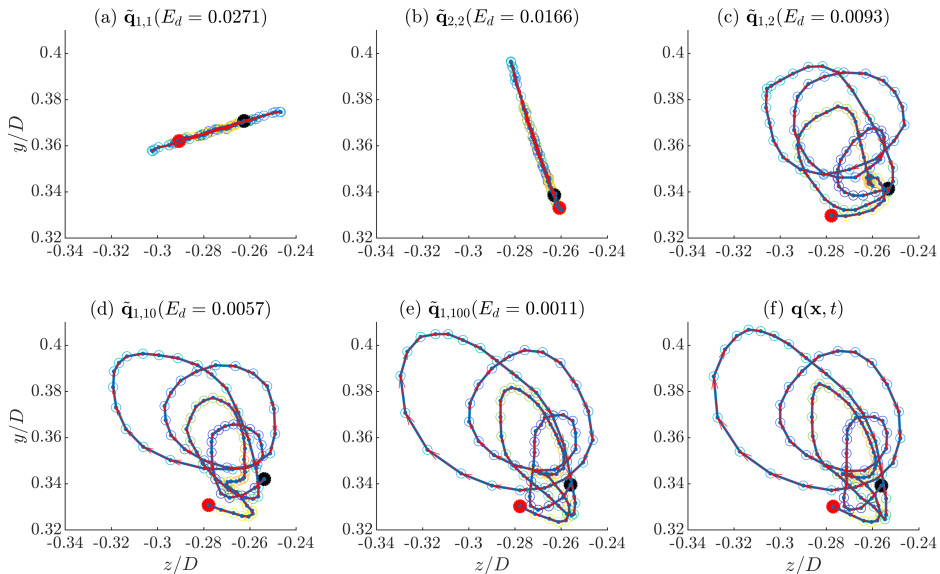


Figure 24: Meandering of the **L**-vortex using reconstructed flow fields. Black and red circles indicate the beginning and the end of the meandering trajectory.

where y_i, z_i are the coordinates of the vortex center from the LES flowfield for snapshots $i = 1, 2, \dots, N$. The tilde quantities (\tilde{y}_i, \tilde{z}_i) represent the vortex centers in the reconstructed flowfield. These errors are also shown in Fig. 24. This error is 0.0271 and 0.0166 considering only the first and second mode respectively, and decreases to 0.0093 when both modes are added. When 10 modes are considered (Fig. 24(d)), the trajectory approaches the actual meandering path even further, and the error decreases to $E_d = 0.0057$. Further, when the vortex core movement is computed on a flowfield reconstructed with 100 modes (Fig. 24(e)), the core trajectory nearly mimics the complete meandering path. The addition of high-order modes mainly contributes to correcting the maximum displacement from the mean vortex, while the direction of the core movement is mainly dictated by only two modes.

In order to confirm that this observation also holds true for the **R** vortex, its reconstructed meandering motions are shown in figure 25(a-e). Consistent with the observations for the **L** vortex, linear displacements are observed due to the first and second POD modes in this vortex also, as shown in figure 25(a) and (b) respectively. The inclinations of the linear paths for this vortex are different from those obtained for **L** case of course, since they are aligned with displacements due to the individual modes of the **R** vortex. The displacement errors E_d due to these modes are comparable to each other. The combined displacement effect due to both modes, shown in figure 25(c), again mimics the actual meandering path (figure 25(f)), except for lower maximum displacements. The addition of 8 more modes brings the trajectory closer to the actual meandering path (figure 25(d)), and with a total 100 modes, the paths nearly overlap with each other (figure 25(e)). Although not shown, for locations closer to the body, the reconstruction error of the meandering path using these modes is slightly higher, as expected from their performance in reconstructing spatial structure (figure 23(b)). However, the key observation that they continue to exhibit low-rank behavior remains valid.

The reconstruction of the meandering path with only a few leading modes confirms the

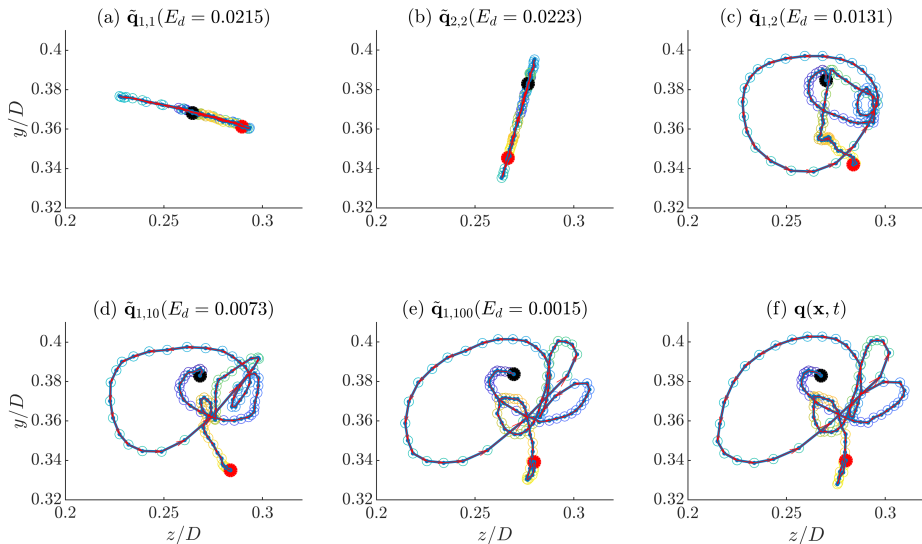


Figure 25: Meandering of **R**-vortex using reconstructed flow fields.

lower-dimensional dynamics and a smaller number of Lyapunov exponents in the dynamical system that characterize the chaos present in the system. Singler (2008) show that POD can be used in the manner above to compute approximate low-rank solutions of the Lyapunov equations. The solution of these equations can be used with standard methods to compute reduced-order models of linear systems either in a Galerkin-based (Couplet *et al.* 2005) or a Galerkin-free approach (Shinde *et al.* 2016). This would constitute a significant step in ultimately determining control laws to modulate the meandering of vortices.

8. Conclusions

High fidelity simulations are employed to examine the dynamics of the flow behind an axisymmetric cylinder with a slanted base. The base upsweep angle considered, $\phi = 20^\circ$, is representative of a cargo fuselage afterbody geometry. The primary feature is a horseshoe-shaped structure that develops around the periphery of the base and ultimately lifts away from the surface to manifest a three-dimensional generally streamwise-oriented vortex pair. Relatively far downstream from the base, these wake vortices, while axisymmetric in the mean sense, exhibit low-frequency meandering in space and time. This motion is characterized by seemingly random displacement of the vortex cores, although the time trajectory of the displacement of the core shows a rotation sense commensurate with the swirl in the vortices. These complex phenomena are first analyzed through proper orthogonal decomposition (POD) at several locations on the ramp as well as downstream of the body. Near the base, the dominant structures show fluctuations in both the vortex and the shear layer. Downstream, however, the coherent structures are characterized by a pair of orthogonal helical modes with azimuthal wave number ($|m| = 1$). These two most energetic modes provide a first-order approximation of the displacement of the vortex cores, confirming that the meandering is primarily associated with changes in large-scale coherent structures. The instability mechanism underlying meandering is analyzed using

a linear stability approach on the time-averaged streamwise vortex pair. The mean vortex obtained from the simulations is first matched to a suitable Batchelor vortex and then a counter-rotating model vortex is placed at an appropriate separation distance from the first vortex. Both spatial and temporal analyses confirm the presence of an elliptic instability with the structures of the unstable modes being similar to those obtained from POD. The unstable modes are obtained at relatively low frequency with the presence of axial velocity as primary mechanism for instability.

Low-rank representation behavior is examined by considering different numbers of POD modes. Consideration of only the first or second mode generates temporal displacement of each core along a relatively straight line, which is very different from the actual meandering path. However, when both the modes are considered together, the effective trajectory recreated recovers the broad meandering motion. In the spatial reconstruction, these two modes alone capture the vortex cores reasonably well, while high-order modes further correct both spatial and temporal reconstructions to capture small scale features. Both spatial and temporal reconstruction errors diminish rapidly with the superposition of additional modes, especially in downstream regions. These low-rank observations of the complex meandering phenomena should facilitate the construction of a reduced-order model as a surrogate for the full dynamical system in flow control analyses.

Acknowledgements

This material is based upon work supported by the Air Force Office of Scientific Research under award number FA9550-17-1-0228 (monitor: Gregg Abate). The authors thank F. Alvi, F. Zigunov, and P. Sellappan for several fruitful communications. Simulations were carried out using resources provided by the U.S. Department of Defense High-Performance Computing Modernization Program and the Ohio Supercomputer Center.

Appendix A. Governing linear stability equations

The incompressible Navier-Stokes equations in non-dimensional form are given by:

$$\nabla \cdot \mathbf{u} = 0 \quad (\text{A } 1)$$

$$\frac{\partial \mathbf{u}}{\partial t} + (\mathbf{u} \cdot \nabla) \mathbf{u} = \nabla p + Re^{-1} \nabla^2 \mathbf{u} \quad (\text{A } 2)$$

where $\mathbf{u} = \{u, v, w\}^T$. The flow field is decomposed into a basic state $(\bar{\mathbf{u}}, \bar{p})$ and perturbations (\mathbf{u}', p') , with the former satisfying equations (A 1). The equations governing linear perturbations are then:

$$\nabla \cdot \mathbf{u}' = 0 \quad (\text{A } 3)$$

$$\frac{\partial \mathbf{u}'}{\partial t} + (\mathbf{u}' \cdot \nabla) \bar{\mathbf{u}} + (\bar{\mathbf{u}} \cdot \nabla) \mathbf{u}' = \nabla p' + Re^{-1} \nabla^2 \mathbf{u}' \quad (\text{A } 4)$$

where the small non-linear terms, $(\mathbf{u}' \cdot \nabla) \mathbf{u}'$, are ignored. For stability analysis, a modal form of the perturbations is assumed, with homogeneity in the x -direction

$$\{u', v', w', p'\}(x, y, z, t) = \{\tilde{u}, \tilde{v}, \tilde{w}, \tilde{p}\}(y, z) e^{i(kx - \omega t)} \quad (\text{A } 5)$$

where the quantities with tilde($\tilde{\bullet}$) are two-dimensional amplitude functions. Substituting this in the perturbation equations (A 3), the stability equations are obtained:

$$\left(\underbrace{\begin{bmatrix} \mathcal{L} & \bar{U}_y & \bar{U}_z & 0 \\ 0 & \mathcal{L} + \bar{V}_y & \bar{V}_z & D_y \\ 0 & \bar{W}_y & \mathcal{L} + \bar{W}_z & D_z \\ 0 & D_y & D_z & 0 \end{bmatrix}}_{\mathbb{A}_0} + k \underbrace{\begin{bmatrix} i\bar{U} & 0 & 0 & i \\ 0 & i\bar{U} & 0 & 0 \\ 0 & 0 & i\bar{U} & 0 \\ i & 0 & 0 & 0 \end{bmatrix}}_{\mathbb{A}_1} + k^2 \underbrace{\begin{bmatrix} IRe^{-1} & 0 & 0 & 0 \\ 0 & IRe^{-1} & 0 & 0 \\ 0 & 0 & IRe^{-1} & 0 \\ 0 & 0 & 0 & 0 \end{bmatrix}}_{\mathbb{A}_2} - \omega \underbrace{\begin{bmatrix} i & 0 & 0 & 0 \\ 0 & i & 0 & 0 \\ 0 & 0 & i & 0 \\ 0 & 0 & 0 & 0 \end{bmatrix}}_{\mathbb{B}} \right) \begin{bmatrix} \tilde{u} \\ \tilde{v} \\ \tilde{w} \\ \tilde{p} \end{bmatrix} = 0 \quad (\text{A } 6)$$

where

$$\mathcal{L} = \bar{V}D_y + \bar{W}D_z - \frac{D_{yy} + D_{zz}}{Re}. \quad (\text{A } 7)$$

D_y, D_{yy} etc. represent first and second-order differentiation matrices. I is the identity matrix.

For the temporal analysis, the real wavenumber k is specified, while $\omega = \omega_r + i\omega_i$ is a complex quantity denoting the circular frequency, ω_r , and growth rate, ω_i . The generalized eigenvalue problem, following equations (A 6), is then:

$$\mathbb{A}\tilde{\mathbf{q}} = \omega\mathbb{B}\tilde{\mathbf{q}}, \quad (\text{A } 8)$$

with $\tilde{\mathbf{q}} = \{\tilde{u}, \tilde{v}, \tilde{w}, \tilde{p}\}^T$ and $\mathbb{A} = \mathbb{A}_0 + k\mathbb{A}_1 + k^2\mathbb{A}_2$.

For spatial stability analysis, the streamwise wavenumber $k = k_r + ik_i$ represents the complex eigenvalue, with $k_i < 0$ indicating spatial exponential growth, and ω is a real specified circular frequency. In this case, equations (A 6) present a quadratic eigenvalue problem:

$$(\mathbb{A}'_0 + k\mathbb{A}_1 + k^2\mathbb{A}_2)\tilde{\mathbf{q}} = 0 \quad (\text{A } 9)$$

with $\mathbb{A}'_0 = \mathbb{A}_0 - \omega\mathbb{B}$.

Although the problem can be solved directly, the quadratic eigenvalue problem can become very expensive for large matrices. Therefore, it is converted into a linear eigenvalue problem by using the companion matrix technique (Tisseur & Meerbergen 2001). The matrix size of this spatial eigenvalue problem is therefore 75% higher than the temporal approach due to the padding of three auxiliary variables at every grid point. For both temporal and spatial analysis, distant farfield boundaries are used to allow for homogeneous Dirichlet boundary conditions for all perturbation variables except for pressure, for which the Neumann boundary condition is appropriate. The eigenvalue problems are solved using the iterative Arnoldi (Arnoldi 1951) algorithm. Further, the shift-and-invert approach (Lehoucq *et al.* 1998) in the Arnoldi algorithm is used to obtain faster convergence to desired eigenvalues. A large Krylov dimension ($k = 100$) is chosen to ensure that the relevant unstable eigenspectrum around the shift value is captured.

- ANTKOWIAK, ARNAUD & BRANCHER, PIERRE 2004 Transient energy growth for the lamb–oseen vortex. *Physics of Fluids* **16** (1), L1–L4.
- ARNOLDI, WALTER EDWIN 1951 The principle of minimized iterations in the solution of the matrix eigenvalue problem. *Quarterly of Applied Mathematics* **9** (1), 17–29.
- AUBRY, NADINE 1991 On the hidden beauty of the proper orthogonal decomposition. *Theoretical and Computational Fluid Dynamics* **2** (5-6), 339–352.
- BAKER, GR, BARKER, SJ, BOFAH, KK & SAFFMAN, PG 1974 Laser anemometer measurements of trailing vortices in water. *Journal of Fluid Mechanics* **65** (2), 325–336.
- BEAM, RICHARD M & WARMING, ROBERT F 1976 An implicit finite-difference algorithm for hyperbolic systems in conservation-law form. *Journal of Computational Physics* **22** (1), 87–110.
- BELL, JR, BURTON, D, THOMPSON, MC, HERBST, AH & SHERIDAN, J 2016 Dynamics of trailing vortices in the wake of a generic high-speed train. *Journal of Fluids and Structures* **65**, 238–256.
- BERESH, STEVEN J, HENFLING, JOHN F & SPILLERS, RUSSELL W 2010 Meander of a fin trailing vortex and the origin of its turbulence. *Experiments in Fluids* **49** (3), 599–611.
- BRION, VINCENT, DEKERRET, HUGUES, SIPP, DENIS & JACQUIN, LAURENT 2008 Optimal perturbation of a vortex sheet for fast destabilization of the trailing vortices. In *38th Fluid Dynamics Conference and Exhibit*, p. 4182.
- BRITCHER, COLIN P & ALCORN, CHARLES W 1991 Interference-free measurements of the subsonic aerodynamics of slanted-base ogive cylinders. *AIAA Journal* **29** (4), 520–525.
- BULATHSINGHALA, DS, JACKSON, RICHARD, WANG, ZHIJIN & GURSUL, ISMET 2017 Afterbody vortices of axisymmetric cylinders with a slanted base. *Experiments in Fluids* **58** (5), 60.
- BULATHSINGHALA, DS, WANG, ZHIJIN & GURSUL, ISMET 2019 Modified near-wakes of axisymmetric cylinders with slanted base. *Aerospace Science and Technology* .
- BURY, YANNICK, JARDIN, THIERRY & KLÖCKNER, ANDREAS 2013 Experimental investigation of the vortical activity in the close wake of a simplified military transport aircraft. *Experiments in Fluids* **54** (5), 1524.
- CHENG, ZE-PENG, QIU, SI-YI, XIANG, YANG & LIU, HONG 2019 Quantitative features of wingtip vortex wandering based on the linear stability analysis. *AIAA Journal* pp. 2694–2709.
- CHOW, JIM S, ZILLIAC, GREGORY G & BRADSHAW, PETER 1997 Mean and turbulence measurements in the near field of a wingtip vortex. *AIAA journal* **35** (10), 1561–1567.
- CORSIGLIA, VR, SCHWIND, RG & CHIGIER, NA 1973 Rapid scanning, three-dimensional hot-wire anemometer surveys of wing-tip vortices. *Journal of Aircraft* **10** (12), 752–757.
- COUPLET, M, BASDEVANT, C & SAGAUT, P 2005 Calibrated reduced-order pod-galerkin system for fluid flow modelling. *Journal of Computational Physics* **207** (1), 192–220.
- CROW, STEVEN C 1970 Stability theory for a pair of trailing vortices. *AIAA Journal* **8** (12), 2172–2179.
- DEL PINO, C, LOPEZ-ALONSO, JM, PARRAS, L & FERNANDEZ-FERIA, R 2011 Dynamics of the wing-tip vortex in the near field of a naca 0012 aerofoil. *The Aeronautical Journal* **115** (1166), 229–239.
- DEVENPORT, WILLIAM J, RIFE, MICHAEL C, LIAPIS, STERGIOS I & FOLLIN, GORDON J 1996 The structure and development of a wing-tip vortex. *Journal of Fluid Mechanics* **312**, 67–106.
- EDSTRAND, ADAM M, DAVIS, TIMOTHY B, SCHMID, PETER J, TAIRA, KUNIHICO & CATTAFESTA, LOUIS N 2016 On the mechanism of trailing vortex wandering. *Journal of Fluid Mechanics* **801**.
- EDSTRAND, ADAM M, SCHMID, PETER J, TAIRA, KUNIHICO & CATTAFESTA, LOUIS N 2018 A parallel stability analysis of a trailing vortex wake. *Journal of Fluid Mechanics* **837**, 858–895.
- EPSTEIN, RONALD J, CARBONARO, MARIO C & CAUDRON, F 1994 Experimental investigation of the flowfield about an unswept afterbody. *Journal of Aircraft* **31** (6), 1281–1290.
- FABRE, DAVID, JACQUIN, LAURENT & LOOF, ANTOINE 2002 Optimal perturbations in a four-vortex aircraft wake in counter-rotating configuration. *Journal of Fluid Mechanics* **451**, 319.

- FAHY, EDWARD F & KARIORIS, FRANK G 1952 Geometrical and graphical representations of lissajous figures. *American Journal of Physics* **20** (3), 121–123.
- FEYS, JAN & MASLOWE, SHERWIN A 2016 Elliptical instability of the moore–saffman model for a trailing wingtip vortex. *Journal of Fluid Mechanics* **803**, 556–590.
- GAITONDE, DATTA V & VISBAL, MIGUEL R 1998 High-order schemes for navier-stokes equations: algorithm and implementation into fdl3di. *Tech. Rep.*. Air Force Research Lab Wright-Patterson AFB OH Air Vehicles Directorate.
- GARMANN, DANIEL J. & VISBAL, MIGUEL R. 2019 High-fidelity simulations of afterbody vortex flows. *AIAA Journal* **57** (9), 3980–3990.
- GONZÁLEZ, LEO M, GÓMEZ-BLANCO, RAFAEL & THEOFILIS, VASSILIS 2008 Eigenmodes of a counter-rotating vortex dipole. *AIAA Journal* **46** (11), 2796–2805.
- GORDNIER, RAYMOND E & VISBAL, MIGUEL R 2005 Compact difference scheme applied to simulation of low-sweep delta wing flow. *AIAA Journal* **43** (8), 1744–1752.
- GRAFTIEAUX, LAURENT, MICHARD, MARC & GROSJEAN, NATHALIE 2001 Combining piv, pod and vortex identification algorithms for the study of unsteady turbulent swirling flows. *Measurement Science and Technology* **12** (9), 1422.
- GREEN, SI & ACOSTA, AJ 1991 Unsteady flow in trailing vortices. *Journal of Fluid Mechanics* **227**, 107–134.
- GUPTA, VIKRANT & WAN, MINPING 2019 Low-order modelling of wake meandering behind turbines. *Journal of Fluid Mechanics* **877**, 534–560.
- GURSUL, I., GORDNIER, R. & VISBAL, M. 2005 Unsteady aerodynamics of nonslender delta wings. *Progress in Aerospace Sciences* **41** (7), 515–557.
- HALLER, GEORGE 2005 An objective definition of a vortex. *Journal of Fluid Mechanics* **525**, 1–26.
- HEIN, S & THEOFILIS, VASSILIOS 2004 On instability characteristics of isolated vortices and models of trailing-vortex systems. *Computers & Fluids* **33** (5-6), 741–753.
- HOLZÄPFEL, FRANK N, STRAUSS, LUKAS & SCHWARZ, CARSTEN W 2019 Assessment of dynamic pairwise wake vortex separations for approach and landing at Vienna airport. In *AIAA Aviation 2019 Forum*, p. 3178.
- IUNGO, GIACOMO V, SANTONI-ORTIZ, C, ABKAR, MAHDI, PORTÉ-AGEL, FERNANDO, ROTEÀ, MARIO A & LEONARDI, STEFANO 2015 Data-driven reduced order model for prediction of wind turbine wakes. In *Journal of Physics: Conference Series*, , vol. 625, p. 012009. IOP Publishing.
- JACKSON, RICHARD, WANG, ZHIJIN & GURSUL, ISMET 2020 Control of upswept afterbody vortices using continuous and pulsed blowing. *Journal of Aircraft* **57** (1), 76–92.
- JACKSON, RICHARD W, WANG, ZHIJIN & GURSUL, ISMET 2015 Control of afterbody vortices by blowing. In *45th AIAA Fluid Dynamics Conference*, p. 2777.
- JACQUIN, LAURENT, FABRE, DAVID, GEFFROY, P & COUSTOLS, E 2001 The properties of a transport aircraft wake in the extended near field-an experimental study. In *39th Aerospace Sciences Meeting and Exhibit*, p. 1038.
- JACQUIN, LAURENT, FABRE, DAVID, SIPP, DENIS & COUSTOLS, ERIC 2005 Unsteadiness, instability and turbulence in trailing vortices. *Comptes Rendus Physique* **6** (4-5), 399–414.
- JOVANOVIĆ, MIHAILO R, SCHMID, PETER J & NICHOLS, JOSEPH W 2014 Sparsity-promoting dynamic mode decomposition. *Physics of Fluids* **26** (2), 024103.
- JUGIER, RÉMI, FONTANE, JÉRÔME, JOLY, LAURENT & BRANCHER, PIERRE 2020 Linear two-dimensional stability of a lamb-oseen dipole as an aircraft wake model. *Physical Review Fluids* **5** (1), 014701.
- KARAMI, MOHAMMAD, HANGAN, H, CARASSALE, L & PEERHOSSAINI, H 2019 Coherent structures in tornado-like vortices. *Physics of Fluids* **31** (8), 085118.
- KERSWELL, RICHARD R 2002 Elliptical instability. *Annual Review of Fluid Mechanics* **34** (1), 83–113.
- LACAZE, LAURENT, BIRBAUD, ANNE-LAURE & LE DIZÈS, STÉPHANE 2005 Elliptic instability in a rankine vortex with axial flow. *Physics of Fluids* **17** (1), 017101–017101.
- LEHOUCQ, RICHARD B, SORENSEN, DANNY C & YANG, CHAO 1998 *ARPACK users' guide: solution of large-scale eigenvalue problems with implicitly restarted Arnoldi methods*. SIAM.

- LEWEKE, THOMAS, LE DIZES, STÉPHANE & WILLIAMSON, CHARLES HK 2016 Dynamics and instabilities of vortex pairs. *Annual Review of Fluid Mechanics* **48**, 507–541.
- LEWEKE, THOMAS & WILLIAMSON, CHARLES HK 1998 Cooperative elliptic instability of a vortex pair. *Journal of Fluid Mechanics* **360**, 85–119.
- LIENHART, H, STOOT, C & BECKER, S 2002 Flow and turbulence structures in the wake of a simplified car model (ahmed model). In *New Results in Numerical and Experimental Fluid Mechanics III*, pp. 323–330. Springer.
- LOMBARD, JEAN-ELOI W, MOXEY, DAVID, SHERWIN, SPENCER J, HOESSLER, JULIEN FA, DHANDAPANI, SRIDAR & TAYLOR, MARK J 2016 Implicit large-eddy simulation of a wingtip vortex. *AIAA Journal* **54** (2), 506–518.
- MA, BAO-FENG, WANG, ZHIJIN & GURSUL, ISMET 2017 Symmetry breaking and instabilities of conical vortex pairs over slender delta wings. *Journal of Fluid Mechanics* **832**, 41–72.
- MATHEW, J., LECHNER, R., FOYSI, H., SESTERHENN, J. & FRIEDRICH, R. 2003 An explicit filtering method for large eddy simulation of compressible flows. *Phys. Fluids* **15** (8), 2279–2289.
- MAYER, ERNST W & POWELL, KENNETH G 1992 Viscous and inviscid instabilities of a trailing vortex. *Journal of Fluid Mechanics* **245**, 91–114.
- MOREL, T 1978 The effect of base slant on the flow pattern and drag of three-dimensional bodies with blunt ends. In *Aerodynamic Drag Mechanisms of Bluff Bodies and Road Vehicles*, pp. 191–226. Springer.
- MULA, SWATHI M & TINNEY, CHARLES E 2015 A study of the turbulence within a spiralling vortex filament using proper orthogonal decomposition. *Journal of Fluid Mechanics* **769**, 570–589.
- NAVROSE, BRION, V & JACQUIN, L 2019 Transient growth in the near wake region of the flow past a finite span wing. *Journal of Fluid Mechanics* **866**, 399–430.
- PAEDES, PEDRO 2014 Advances in global instability computations: from incompressible to hypersonic flow. *Universidad Politécnica de Madrid: PhD Dissertation*.
- PAEDES, PEDRO, THEOFILIS, VASSILIOS, RODRIGUEZ, DANIEL & TENDERO, J 2011 The pse-3d instability analysis methodology for flows depending strongly on two and weakly on the third spatial dimension. In *6th AIAA Theoretical Fluid Mechanics Conference*, p. 3752.
- PARRAS, LUIS & FERNANDEZ-FERIA, RAMON 2007 Spatial stability and the onset of absolute instability of batchelor’s vortex for high swirl numbers. *Journal of Fluid Mechanics* **583**, 27–43.
- PULLIAM, THOMAS H & CHAUSSEE, DS 1981 A diagonal form of an implicit approximate-factorization algorithm. *Journal of Computational Physics* **39** (2), 347–363.
- RANJAN, RAJESH, AULTMAN, MATTHEW & GAITONDE, DATTA 2020 Mean flowfield evolution with upsweep angle in a simulated cargo fuselage aftbody. *Journal of Aircraft* **57** (6), 1156–1169.
- RANJAN, RAJESH & GAITONDE, DATTA 2020 Hysteresis in slanted-base-cylinder afterbody flows. *Aerospace Science and Technology* **106**, 106138.
- ROSSITTO, GIACOMO, SICOT, CHRISTOPHE, FERRAND, VALÉRIE, BORÉE, JACQUES & HARAMBAT, FABIEN 2016 Influence of afterbody rounding on the pressure distribution over a fastback vehicle. *Experiments in Fluids* **57** (3), 43.
- ROWLEY, CLARENCE W, COLONIUS, TIM & MURRAY, RICHARD M 2004 Model reduction for compressible flows using pod and galerkin projection. *Physica D: Nonlinear Phenomena* **189** (1-2), 115–129.
- SHINDE, VILAS, LONGATTE, ELISABETH, BAJ, FRANCK, HOARAU, YANNICK & BRAZA, MARIANNA 2016 A galerkin-free model reduction approach for the navier–stokes equations. *Journal of Computational Physics* **309**, 148–163.
- SINGLER, JOHN R 2008 Approximate low rank solutions of lyapunov equations via proper orthogonal decomposition. In *2008 American Control Conference*, pp. 267–272. IEEE.
- SIPP, DENIS & JACQUIN, LAURENT 2003 Widnall instabilities in vortex pairs. *Physics of Fluids* **15** (7), 1861–1874.
- SIROVICH, LAWRENCE 1987 Turbulence and the dynamics of coherent structures. i. coherent structures. *Quarterly of Applied Mathematics* **45** (3), 561–571.
- TISSEUR, FRANÇOISE & MEERBERGEN, KARL 2001 The quadratic eigenvalue problem. *SIAM Review* **43** (2), 235–286.

- TSAI, CHON-YIN & WIDNALL, SHEILA E 1976 The stability of short waves on a straight vortex filament in a weak externally imposed strain field. *Journal of Fluid Mechanics* **73** (4), 721–733.
- VISBAL, MIGUEL R & GAITONDE, DATTA V 2002 On the use of higher-order finite-difference schemes on curvilinear and deforming meshes. *Journal of Computational Physics* **181** (1), 155–185.
- WIDNALL, SE, BLISS, D & ZALAY, A 1971 Theoretical and experimental study of the stability of a vortex pair. In *Aircraft wake turbulence and its detection*, pp. 305–338. Springer.
- YANIKTEPE, B & ROCKWELL, D 2004 Flow structure on a delta wing of low sweep angle. *AIAA Journal* **42** (3), 513–523.
- ZEMAN, O 1995 The persistence of trailing vortices: a modeling study. *Physics of Fluids* **7** (1), 135–143.
- ZHANG, XIZHE, WANG, ZHIJIN & GURSUL, ISMET 2016 Interaction of multiple vortices over a double delta wing. *Aerospace Science and Technology* **48**, 291–307.
- ZIGUNOV, FERNANDO, SELLAPPAN, PRABU & ALVI, FARRUKH S 2020a Dynamics of the slanted cylinder afterbody vortices. In *AIAA Scitech 2020 Forum*, p. 1322.
- ZIGUNOV, F., SELLAPPAN, P. & ALVI, F. S. 2020b Reynolds number and slant angle effects on the flow over a slanted cylinder afterbody. *Journal of Fluid Mechanics* **891**.